frontiers | Frontiers in Chemistry

TYPE Review
PUBLISHED 22 August 2022
DOI 10.3389/fchem.2022.978078

OPEN ACCESS

EDITED BY
Tiancheng Mu,
Renmin University of China, China

REVIEWED BY
Baowen Zhou,
Shanghai Jiao Tong University, China
Tianbin Wu,
Institute of Chemistry (CAS), China

*CORRESPONDENCE
Leiduan Hao,
haold@mail.buct.edu.cn
Zhenyu Sun,
sunzy@mail.buct.edu.cn

SPECIALTY SECTION
This article was submitted to Green and Sustainable Chemistry, a section of the journal Frontiers in Chemistry

RECEIVED 25 June 2022
ACCEPTED 15 July 2022
PUBLISHED 22 August 2022

CITATION
Hui X, Wang L, Yao Z, Hao L and Sun Z (2022), Recent progress of photocatalysts based on tungsten and related metals for nitrogen reduction to ammonia.
Front. Chem. 10:978078.
doi: 10.3389/fchem.2022.978078

Recent progress of photocatalysts based on tungsten and related metals for nitrogen reduction to ammonia

Xiangchao Hui, Lijun Wang, Zhibo Yao, Leiduan Hao* and Zhenyu Sun*

State Key Laboratory of Organic-Inorganic Composites, College of Chemical Engineering, Beijing University of Chemical Technology, Beijing, China

Photocatalytic nitrogen reduction reaction (NRR) to ammonia holds a great promise for substituting the traditional energy-intensive Haber–Bosch process, which entails sunlight as an inexhaustible resource and water as a hydrogen source under mild conditions. Remarkable progress has been achieved regarding the activation and solar conversion of N_2 to NH_3 with the rapid development of emerging photocatalysts, but it still suffers from low efficiency. A comprehensive review on photocatalysts covering tungsten and related metals as well as their broad ranges of alloys and compounds is lacking. This article aims to summarize recent advances in this regard, focusing on the strategies to enhance the photocatalytic performance of tungsten and related metal semiconductors for the NRR. The fundamentals of solar-to-NH_3 photocatalysis, reaction pathways, and NH_3 quantification methods are presented, and the concomitant challenges are also revealed. Finally, we cast insights into the future development of sustainable NH_3 production, and highlight some potential directions for further research in this vibrant field.

KEYWORDS

photocatalysis, nitrogen reduction, ammonia synthesis, tungsten, semiconductor

1 Introduction

As the cornerstone of modern civilization, ammonia (NH_3) is an incontrovertible raw material for modern industry and agriculture, which plays a crucial role in human survival and economic growth. Moreover, due to its high hydrogen content (17.7 wt%), gravimetric energy density (3 kWh kg^{-1}) and easy liquification (−33°C under atmospheric pressure), NH_3 also serves as a useful commodity for chemicals used in industries and as a carbon-free clean energy carrier (Guo and Chen, 2017). NH_3 is by far predominantly fabricated via the energy- and capital-intensive Haber-Bosch process requiring extreme reaction conditions of 300–500°C and 15–25 MPa, which gives rise to excessive consumption of feedstocks and consequently high CO_2 emissions. Therefore, exploring and developing renewable, environment-friendly, and green routes to yield NH_3 is desirable. Photocatalytic N_2 fixation is perceived as an alternative sustainable

strategy for facile, cost-effective ammonia production using water and nitrogen gas under ambient conditions. There is enormous, acknowledged and untapped potential in this emerging field. Considering that nitrogen reduction reaction (NRR) coupled with water oxidation is a thermodynamically uphill reaction, solar energy is hence crucial to induce incoming photons generating electronic charge carriers to initiate the catalytic reaction. Since the pioneering research by Schrauzer and co-workers embarked on the photocatalytic reduction of N_2 to NH_3 by employing TiO_2-based photocatalysts (Schrauzer and Guth, 1977), explorative efforts in this sector have been exerted to develop novel photocatalysts with high efficiency, especially in recent years (Schrauzer and Guth, 2002). The initial attempts are currently expanded to widen the scope of investigated materials and their modifications, as well as effective strategies of tuning crystalline phase, surface defects, heteroatom doping, surface modification and/or heterostructure construction for enhancing photocatalytic performances. The photochemical process underpins the terms of selectivity, efficiency, and low operational cost for the production of NH_3 toward the practical implementation at relatively ambient conditions using solar energy. Despite the huge potentials, the photocatalytic NH_3 production still falls far short of the ideal of being commercialized, which results from weak adsorption/activation of the nonpolar N≡N triple bond of N_2 (941 kJ mol^{-1}), inefficient light absorption, and poor photo-induced charge separation (Shen et al., 2021).

Design and development of efficient photocatalysts hold the key to achieve improved performance of photocatalytic NRR. To date, several prior articles (Chen et al., 2018; Shi et al., 2019; Shuai Zhang et al., 2019; Huang et al., 2020; Chen-Xuan Xu et al., 2021; Lee et al., 2021; Shen et al., 2021; Tong Xu et al., 2021) have outlined the recent advancements of photoreduction of N_2 to NH_3 and photocatalysts engineering strategies. Transition metals, especially the early transition metals (e.g., tungsten, molybdenum, vanadium etc.), which possess both empty orbitals and abundant *d*-orbital electrons as well as suitable bandgap energies, could activate dinitrogen molecules through σ-donation/π-backdonation effects, showing huge potential for applications as photocatalysts for photocatalytic NRR. However, few reviews, to the best of our knowledge, have hitherto summarized tungsten and related metals photocatalysts together with a specific focus on strategies to enhance their performances. This review elaborated the state-of-the-art understanding of the basic principles of NRR photocatalysis, reaction mechanisms, thermodynamic limits, and enforceable protocols involved in the overall photochemical processes. We comprehensively discuss recent progress over semiconductors containing tungsten (W), molybdenum (Mo), cobalt (Co), vanadium(V), tantalum (Ta), niobium (Nb), rhenium (Re), zirconium (Zr), hafnium (Hf), and their major advantages as to photocatalysis activity. Furthermore, we emphasize several strategies to improve the photocatalytic performance and also highlight the challenges and future directions for sustainable NH_3 production.

2 Fundamentals for photochemical NRR

2.1 Properties of N_2 molecules

Molecular dinitrogen possesses a triple bond between the nitrogen atoms and a non-bonding pair of electrons on each atom. Atomic nitrogen has 5 valence electrons and 4 valence orbitals (2*s*, $2p_x$, $2p_y$, and $2p_z$), whereas hybridization of the *s-p* atomic orbitals of N_2 consists of four bonding orbitals (two σ and two π orbitals) and four antibonding orbitals (two σ^* and two π^* orbitals). The electrons from the π and 2σ orbitals are shared to form N≡N bond leaving these from $1\sigma^*$ and 1σ orbitals the non-bonding electron pairs (Figure 1A) (Kitano et al., 2012). Hence, the large energy gap of 10.82 eV between the highest occupied molecular orbital (HOMO) and lowest unoccupied molecular orbital (LUMO) seriously hinders electron injection into N_2 antibonding orbitals (Jia and Quadrelli, 2014). A strong N≡N bond energy (945 kJ mol^{-1}) and first-bond breaking energy (410 kJ mol^{-1}) render N_2 molecules extremely thermodynamically stable (Gambarotta and Scott, 2004), meanwhile, N_2 molecules are chemically inert by virtue of high ionization energy of 15.85 eV and negative electron affinity of −1.9 eV (Figure 1B). Therefore, adsorption and dissociation of N_2 with weak polarizability and lacking dipole moment are widely regarded to be the rate-determining steps of NRR (Guo et al., 2018; Liang Yang et al., 2020; Yi-Fei Zhang et al., 2020). Both computational and experimental works have demonstrated that transition metal-based materials interact strongly with N_2 through the formation of N–metal bonds, thanks to the empty *d* orbitals in the transition metals (TMs) accepting the lone pair electrons of N_2 and back donating *d-p* electrons into the anti-binding orbitals of N_2 based on an "acceptance-donation" protocol, whereby the triple bond can be weakened and activated to facilitate the bond dissociation (Figure 1C). Some advances have demonstrated the incomparable advantages of *d* block compounds, but this realm remains elusive.

2.2 Principles and mechanisms of photochemical NRR to NH_3

Ideally, photocatalytic NRR into NH_3 involves transfer of 6 protons and 6electrons, which is a strong endothermic reaction with stoichiometric O_2 production formed by water oxidation (overall reaction: N_2 (g) + $3H_2O$ (l) ↔ $2NH_3$ (g) + $3/2O_2$ (g),

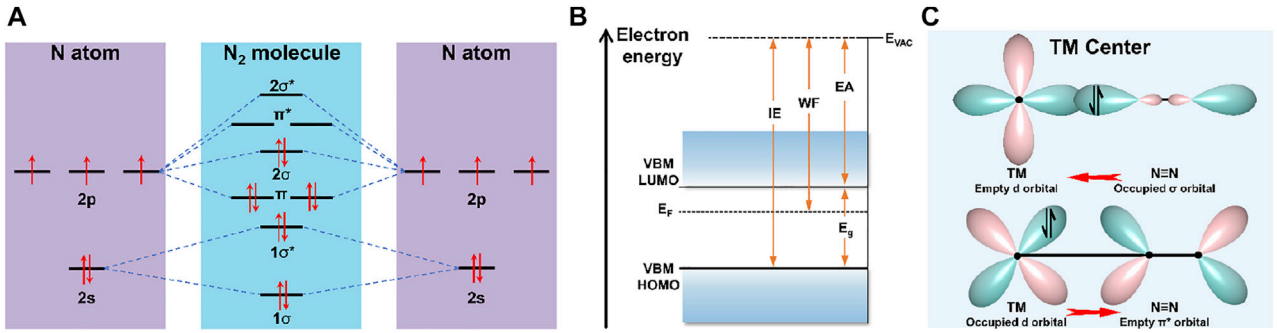

FIGURE 1
(A) Diagram of N atomic orbitals and N_2 molecular orbitals. **(B)** Energy diagram for N_2. E_{VAC}, E_g, WF, IE, EA, and E_F represent vacuum level, energy gap, work function, ionization energy, electron affinity, and Fermi level, respectively. **(C)** Schematic illustration of N_2 bonded to TMs.

ΔG = +7.03 eV) (Medford and Hatzell, 2017). The photochemical NRR requires a potential of at least 1.17 eV per electron (Comer and Medford, 2018), which is initiated by the absorption of photons with an energy higher than the energy bandgap (E_g) of a semiconductor photocatalyst to generate photoexcited electron-hole pairs and an energy >1.17 eV demanded for the overall NH_3 production (Figure 2A). Upon photo-irradiation with sufficient energy supply, electrons (e^-) leap into the conduction band (CB) with simultaneous generation of holes (h^+) at valence band (VB), thus triggering the reduction of N_2 to NH_3 with photo-excited electrons and water oxidation with created holes (Linsebigler et al., 1995). The photoinduced separation of charge carriers is the prerequisite for all semiconductor photocatalysis. However, the migration and separation of photoexcited electron-hole pairs to the semiconductor surface active sites to participate in the redox reactions competes with their recombination in the bulk and on the surface. Eventually, the reaction products desorb from the photocatalyst surface and are transferred to the medium to close the cycle (Figure 2B). Note that the NRR is an uphill reaction. As a consequence, the CB and VB positions of a photocatalyst must bestride the reduction potential of N_2 and the oxidation potential of H_2O. Theoretically, the bottom of the CB should be more negative than the reduction potential of N_2/N_2H (−3.2 V vs. normal hydrogen electrode, NHE), while the top of VB must be beyond the oxidation potential of H_2O/O_2 (+1.23 V vs. NHE). Satisfying both of the above requirements with a singular conventional semiconductor seems to be incompatible, which is unfavorable for harvesting most of the light across the solar spectrum. Since a considerable number of electron-hole pairs recombine inside or on the surface of the catalyst with a rather fast kinetics rate (Zhang et al., 2012), or dissipate in the form of heat or light energy, thus resulting in a decrease of reaction efficiency. Accordingly, most of the reported catalysts for photocatalytic NH_3 production still suffer from low light utilization, fast recombination of photoexcited electron-hole pairs, poor N_2 adsorption/activation, and sluggish electron-to-N_2 transfer kinetics, hobbling the overall solar-to-ammonia conversion efficiency. Additionally, the insufficient stability of the photocatalysts is another serious issue. Many semiconductors could undergo photo-corrosion upon light irradiation, which can be induced by the photo-generated electrons or holes, thus leading to degradation of NRR performance and inhibiting the long-time photocatalytic ammonia synthesis.

The current well-established mechanisms for photocatalytic NRR can be roughly divided into the following: dissociative, associative or enzymatic pathways as shown in Figure 3 (van der Ham et al., 2014; Hao Li et al., 2016; Shipman and Symes, 2017). For the dissociative pathway, the breaking of the N≡N bond precedes the hydrogenation process, followed by the stepwise protonation of the adsorbed nitrogen atoms to form NH_3, analogous to the reaction mechanism of the industrial Haber-Bosch process (Garden and Skulason, 2015), which is however unfavorable for N_2 photoreduction to NH_3 resulting from the large external energy input required for the cleavage of the N≡N triple bond (Shipman and Symes, 2017). According to the different hydrogenation sequences, the associative N_2 reduction mechanism follows either distal pathway or alternating pathway. In the distal associative pathway, the nitrogen atom far from the adsorption site is protonated successively before generating the first NH_3 molecule, leaving another N atom to yield the second NH_3 molecule. Conversely, in the alternate pathway, the hydrogenation reaction occurs alternately at two nitrogen atoms, each of which could react with injected electrons and protons, forming key intermediates such as metal-bound diazene (HN = NH) and reaction byproducts such as N_2H_4 (Bo et al., 2021). As for the enzymatic pathway, the 2 N atoms of the nitrogen molecule are simultaneously adsorbed by the

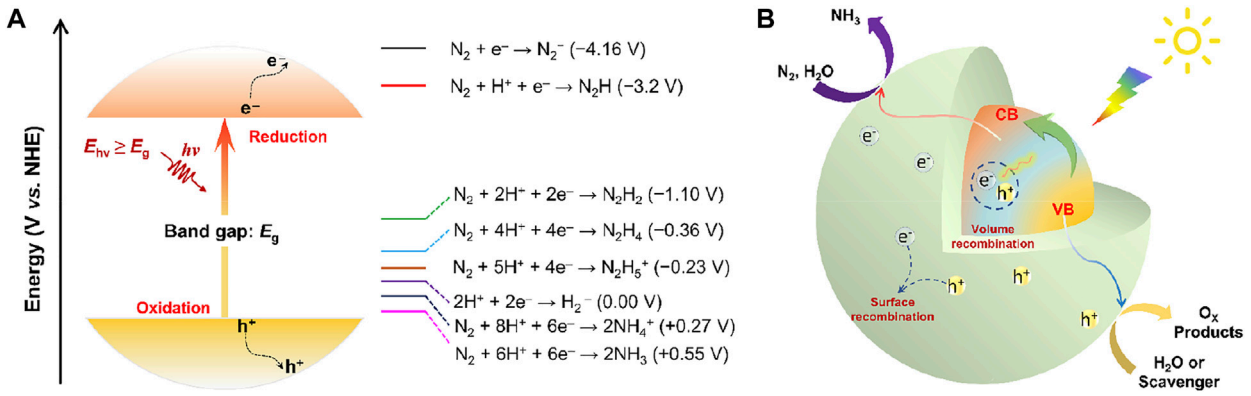

FIGURE 2
(A) Schematic energy diagram related to the reduction of N_2 to NH_3. **(B)** Schematic illustration of the complete photocatalytic NH_3 synthesis over semiconductor-based photocatalysts.

active center of the catalyst, anchored on the catalyst surface via the "side-on" configuration, and then hydrogenated (Hinnemann and Norskov, 2006; Xiao-Fei Li et al., 2016). The proposal that gained the widest support was that photocatalytic NH_3 synthesis follows associative pathways, during which the adsorption and activation of N_2 and then the transfer of photogenerated electrons from the photocatalyst to N_2 provide a lower reaction energy barrier for the dissociation of N≡N triple bonds (Montoya et al., 2015). The activation of N_2 involves the formation of a coordinate bond with the active site proceeded on a catalytic surface, and the subsequent electron transfer and protonation are the keys to weakening the N≡N bonding energy (Jacobsen et al., 2001). Different mechanisms have been proposed, but deep mechanistic understanding of NRR that may vary for distinct catalytic systems remains to be further explored.

2.3 Thermodynamic limits of photocatalytic NRR to NH_3

Due to the proton-electron transfer of multiple intermediates resulting in sluggish reaction kinetics, the thermodynamic constraints relying on the reaction intermediates and the overall and half-reaction thermodynamics independent of the photocatalysts play the decisive role in the photocatalytic NRR process (Table 1). Despite the overall reaction of NH_3 production via N_2 reduction in water (N_2 (g) + $6H^+$ + $6e^-$ ↔ $2NH_3$ (g), E^0 = +0.55 V vs. NHE) is more thermodynamically feasible than the competing hydrogen evolution reaction (HER) by water reduction, HER is more likely to occur with fewer electrons, decreasing the selectivity toward NH_3. Besides, the more negative potentials for the intermediate reactions, such

TABLE 1 Thermodynamic potentials of hydrogenation reactions related to the whole nitrogen fixation pathways.

Reaction equilibrium	E^o	Ref.	Eqn.
N_2 (g) + $3H_2O$ (l) ↔ $2NH_3$ (g) + $3/2O_2$ (g)	−1.137 V vs. SHE (pH 0)	Hochman et al. (2020)	1
$2H^+ + 2e^-$ ↔ H_2 (g)	0 V vs. SHE (pH 0)	Shi et al. (2020a)	2
$3H_2O$ (l) ↔ $3/2O_2$ (g) + $6H^+ + 6e^-$	+1.23 V vs. NHE (pH 0)	Hochman et al. (2020)	3
N_2 (g) + $6H^+ + 6e^-$ ↔ $2NH_3$ (aq)	+0.092 V vs. RHE	Lindley et al. (2016)	4
N_2 (g) + $6e^-$ ↔ N_2^- (aq)	−4.16 V vs. NHE or −3.37 V vs. RHE (pH 14)	Shi et al. (2020b)	5
N_2 (g) + $6H^+ + 6e^-$ ↔ $2NH_3$ (g)	+0.55 V vs. NHE (pH 0)	Bazhenova and Shilov, (1995)	6
$N_2 + 8H^+ + 8e^-$ ↔ $2NH_4^+$	+0.27 V vs. NHE (pH 0)	Chen et al. (2018)	7
N_2 (g) + $H^+ + e^-$ ↔ N_2H	−3.20 V vs. RHE	Shi et al. (2020a)	8
$N_2 + 2H^+ + 2e^-$ ↔ N_2H_2 (g)	−1.10 vs. RHE	Shi et al. (2020a)	9
$N_2 + 4H^+ + 4e^-$ ↔ N_2H_4 (g)	−0.36 V vs. RHE	Shi et al. (2020a)	10
N_2H_2 (g) + $2H^+ + 2e^-$ ↔ N_2H_4 (aq)	0.529 vs. RHE	Fu et al. (2022)	12
N_2H_4 (aq) + $2H^+ + 2e^-$ ↔ $2NH_3$ (aq)	0.939 vs. RHE	Fu et al. (2022)	13
N_2 (g) + $6H_2O$ ↔ $2NO_3^-$ + $12H^+ + 10e^-$	+1.24 V vs. NHE	Yifu Chen et al. (2020)	14

as −4.2 V (vs. RHE) for one-electron activation to form surface-bound N_2 and −3.2 V (vs. RHE) for first proton-coupled one-electron hydrogenation of N_2 (Zhu et al., 2013; Shi et al., 2020a; Huang et al., 2020), are beyond the photocatalysis capability of most semiconductors without active sites.

The initial chemisorption and activation of N_2 could trigger the formation of different kinds of species in the subsequent reactions owing to multiple complicated electrons transferred hydrogenation procedures and the presence of reactive oxygen species by water oxidation half-reaction, such as oxygen, hydroxyl radicals ·OH ($2H_2O + 4h^+ \rightarrow O_2 + 4H^+$, $E^0 = 0.81$ V vs. NHE at pH 7 or $H_2O + h^+ \rightarrow OH + H^+$, $E^0 = 2.32$ V vs. NHE at pH 7) (Sun et al., 2018). Adversely, the formed O_2 further captures electrons in the CB to suppress the NH_3 photosynthesis (Shiraishi et al., 2018; Sun et al., 2018), and the strong oxidation agents ·OH can also further generate nitrite or nitrate from the generated NH_3 by photooxidation, which are detrimental to N_2 photoreduction to NH_3. Because of its weaker interaction with the surface O atom caused by vacancies or doping, metal is further less firmly bound to O following the release of one H atom from adsorbed H_2O^* onto the surface O atom, thus two OH* bonded at the neighboring catalytic sites are easily coupled forming peroxide $H_2O_2^*$ preferentially adsorbed at active sites, thereafter poisoning the photocatalyst (Liu et al., 2012). The oxidation half-reaction products also oxidize the photogenerated NH_3 to HNO_3, leading to a decrease in the NH_3 yield. Yang et al. (2021) transformed the N_2 disproportionation reaction into a complete reductive nitrogen photofixation by introducing Au nanoparticles into Fe-TiO_2 to effectively decompose H_2O_2. Some neglected N_2 fixation products (e.g., N_2H_4, NO_2^-, and NO_3^-, etc.) as essential chemicals should be noted (Table 1, Eqs. 10 and 14), in which N_2H_4 as a by-product from aforementioned associative alternating pathways has also been detected in the same research (Schrauzer and Guth, 2002; Xiao-Fei Li et al., 2016). Li et al. (Hao Li et al., 2016) discovered that N_2H_4 was quickly generated over the BiOCl nanosheets exposed with (010) facets and then gradually disappeared to produce NH_3, which strongly supports the alternative mechanism. In terms of thermodynamic potentials (Table 1, Eqs. 9 and 12), N_2H_4 is more prone to be transformed to NH_3 from surface–N_2H_4 intermediates due to its much weaker N–N single bond. Similar to the hydrogenation pathway to NH_3, dissociated adsorbed N_2 molecule is oxidized to the intermediate of metastable NO* by photogenerated h^+, followed by further oxidation with O_2 and H_2O from the reaction media, by which N_2 is converted to nitrate and nitrite through continuous photooxidation reactions (Comer and Medford, 2018). The previously reported N_2 photoreduction products are either NH_4^+ or NO_3^- (Liu et al., 2019; Dong Zhang et al., 2022), simultaneous coproduction of NH_4^+ and NO_3^- through simultaneous reduction and oxidation of N_2 in pure water, which was demonstrated to occur spontaneously in aqueous solutions (Ren et al., 2020). Another critical aspect in NH_3 production via photochemical N_2 reduction is that some key reaction intermediates are instrumental in NH_3 conversion. Zhao et al. (2022) established a redox pathway with a lower kinetic barrier for NH_3 photosynthesis, in which N_2 and O_2 can be trapped at the oxygen vacancies in ultrathin two-dimensional (2D) CuCo metal-organic frameworks (MOFs) to generate *NO and further be reduced to NH_3 by visible light. Although the desired NH_3 conversion and selectivity are swayed by these competing reactions, some by-products also play imperative roles in industrial production and living needs.

The addition of sacrificial agents (typically electron donors such as sulfites, amines, humic acid, ascorbic acid, and alcohols) with oxidation potentials lower than water appeases the requirement for oxidizing ability in some SC photocatalysts, further suppressing electron-hole pair recombination (Shen et al., 2020). On the other hand, the overall production rate of NH_3 is kinetically balanced by the hole consumption rate on the photocatalyst since electrons and holes are generated in pairs under illumination. Organic alcohols with an α-H adjacent to the OH group(s)-to wit, methanol, ethanol, 2-propanol, ethylene glycol, and so forth, can react with holes in VB to accelerate the production of electrons and liberation of protons (Chen et al., 2015). Among them, methanol is demonstrated to be more appropriate and efficient than other hole sacrificial reagents. Methanol not only loses electrons more easily to consume the accumulated holes due to its lower HOMO (Zhao et al., 2015), but also promotes the solubility of N_2, which could act as a proton donor and partial electron donor for subsequent reduction reactions (Li et al., 2018). However, methanol as the sacrificial agent could be oxidized to form carbonyl-containing compounds (e.g., aldehyde or ketone) and finally CO_2, which might interfere with product detection and quantification. The N_2 fixation reaction can also be facilitated by $*CO_2^-$ produced from the oxidation process of methanol (Swain et al., 2020). Cao and co-workers (Cao et al., 2018) found that the·CO_2^- intermediates transformed from methanol or absorbed CO_2 affected the nitrogen fixation due to their strongly reducing ability ($E_{CO2/\cdot CO2-} = 1.8$ V) ($5N_2 + 2CO_2^- + 4H_2O \rightarrow 2NH_3 + 2CO_2 + 2OH^-$) (Dimitrijevic et al., 2011). It should be noted that the NH_3 formation mechanism in such sacrificial systems should be taken with great caution, the target scavenger should be chosen carefully.

2.4 Protocols, evaluation, and detection methods in photocatalytic NRR

Despite the great strides toward photon-driven ammonia production that have been taken, unified rules and standards in this fledgling field should be formulated to ensure the authority and accuracy, by which the impetus imparted forcefully

contribute to advance of the sustainable technology. Since the low NH_3 yield (ppb/ppm level) and ubiquitous contaminants plague experimental practices (Gao et al., 2018; Tang and Qiao, 2019; Zhao et al., 2019), establishing a uniform protocol for rigorous experiments preceding the detection and quantification of NH_3 are noncontroversial. Therefore, to clarify the source of NH_3 and ensure data reproducibility, various contamination sources from the environment, latex gloves, human respiration, stable deionized water, photochemical reactor, or the used feed gas, even NH_3 or amine groups unintentionally introduced by catalysts, should be ruled out to avoid overestimation of the NH_3 concentration (Bai et al., 2017; Zhao et al., 2021). The photocatalysts, photoreaction set-up and all its components as well as sample tubing should be thoroughly rinsed with fresh ultrapure water and properly stored. Particular emphasis should be put on the NO_x contaminants derived from N-containing chemicals, protic solvents, or supply gas, which are easily reduced to NH_3 (Xue Chen et al., 2020; Li et al., 2022a; Feng Wang et al., 2022; Xu et al., 2022). To account for the reliability and repeatability of photoactivity, it is strongly recommended to use reported rigorous experimental protocols (Andersen et al., 2019; Tang and Qiao, 2019; Choi et al., 2020; Shen et al., 2021), which clearly list experimental methods, gas purification, blank and control experiments, especially the isotopic labeling experiments. The $^{14}N_2$ and $^{15}N_2$ feed gases should be pre-purified to remove any possible NO_x or NH_3 to eliminate uncertainty and even false positives of catalytic data (Zhao et al., 2020; Hui et al., 2022; Yuting Wang et al., 2022).

However, controversy exists as to how to obtain reliable detection and quantification of NH_3 and NH_4^+, which severely hampered the growth of this field. Fortunately, the development of measuring techniques further pushed the advance of NH_3 evaluation. Currently, detection and quantification of NH_3 could be mainly divided into five methods, including spectrophotometric/colorimetric assays using indophenol blue or Nessler's reagent, ion chromatography (IC), ion-selective electrode (ISE), fluorescence, and ^{1}H-NMR spectroscopy methods (Gao et al., 2018; Zhao et al., 2019). These methods are methodologically sound and get concordant precise results for NH_3 determination in water systems (Mansingh et al., 2021). However, each of these methods has both advantages and limits for measuring NH_3. Colorimetric assays are widely available with benefits of good sensitivity, fine accuracy (0–500 $\mu g_{NH3}\ L^{-1}$), and low cost (Zhao et al., 2019). The pH, solvent used, presence of certain metal ions, sacrificial agents and their oxides, and nitrogen-containing chemicals can all adversely increase the amount of NH_3 detected by the coloration methods (Gao et al., 2018). IC is recommended for NH_3 quantification given its reproducible, precise results with a wider range of NH_3 estimation, superior efficiency and selectivity, and good stability, but it still suffers from the disadvantage that certain sacrificial agents affect the separation efficiency of the cation-exchange column. NMR spectroscopy, mass spectroscopy, and enzyme assays are also employed as supplementary measures to eliminate the possible false-positive results, the first of which, even quantitatively, could not prove the origin of all ammonia generated. For consistency and scientific rigor, the concentration of NH_3 detected should be cross-checked with two or more different quantitative methods, even conducted in *in-situ* and continuous monitoring processes for reliable evidences from an unimpeachable source.

Given the lack of the standard photocatalytic reaction systems used in conventional laboratory tests (Ziegenbalg et al., 2021), it is therefore necessary to pay particular attention to various vital details during the assessment of photocatalytic nitrogen fixation. Figure 4 presents the effect of important experimental parameters on the observed catalytic performance for photo-driven NH_3 production. An objective and meaningful comparison of photocatalytic NH_3 synthesis performance among different groups is heavily reliant on a set of standard experimental conditions (e.g., light source intensity, irradiation wavelength range, photocatalyst dosage, reaction solution volume, reactor type, reaction temperature and pressure, *etc.*). Many technical aspects especially the light source are often missing or not stated in sufficient details. Standardization of reactor design is desirable, thereby minimizing the impact of geometry. Reported performance evaluation is primarily based on NH_3 yield, apparent quantum yield/efficiency (AQY/AQE) and turnover frequency (TOF). However, mass-based performance metrics (*e.g.*, $\mu mol\ h^{-1}\ g^{-1}$) are insufficient because photocatalytic activity is not necessarily proportional to the catalyst mass (Kramm et al., 2019; Huimin Liu et al., 2021). Similarly, AQY/AQE is often used to evaluate the photocatalytic activity under monochromatic light excitation of the same specific wavelength, which is closely related to the wavelength of incident photons and the intrinsic properties of the materials, since photocatalysts generally behave differently on absorption coefficients and photocatalytic activities at each irradiation wavelength (Yuhua Wang et al., 2019). TOF differs as well in terms of the active centers. Solar-to-NH_3-yield (SAY)/solar-to-NH_3 (STA) efficiency can be universally used as the practical standard for comparison, which is determined by a solar simulator (AM 1.5G) with an irradiance of 100 $mW\ cm^{-2}$. With more regard to normalizing evaluation systems, solar-to-NH_3 energy conversion (SEC) efficiency is suggested to objectively compare the catalytic activity of different materials and assay the future industrialization opportunities (targeted SEC ≈10%) (Rong Zhang et al., 2019; Ziegenbalg et al., 2021).

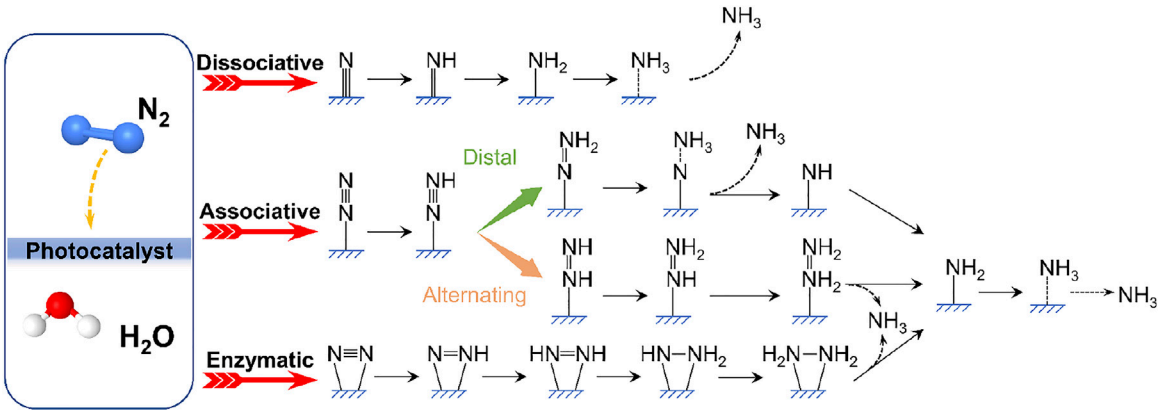

FIGURE 3
Schematic representation of possible pathways for N_2 fixation to NH_3 on catalyst surfaces.

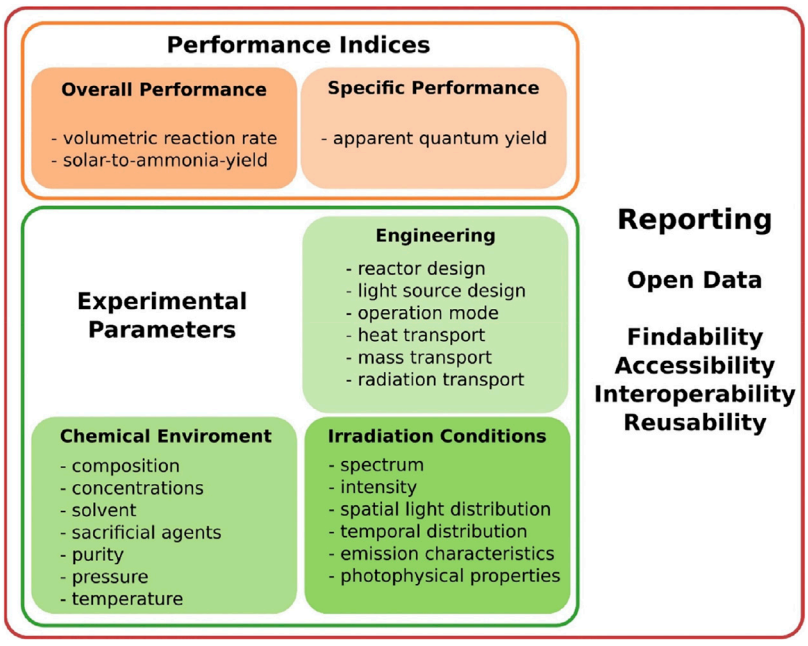

FIGURE 4
Guidelines for experiment normalization to rule out the impact of various parameters that influence the overall and specific performance indices. Reproduced from ref. (Ziegenbalg et al., 2021). With permission from the John Wiley and Sons.

3 Tungsten-based and related photocatalysts for NRR

3.1 Metal oxide-based photocatalysts

3.1.1 Tungsten oxides

Tungsten oxides, commonly denoted as $WO_{3-x}{\cdot}nH_2O$ ($x < 1$, $n = 0$–2), are somewhat distorted in their crystal structure made up of perovskite units, rather not perfect octahedral, with bandgap energies ranging from 2.4 to 2.8 eV depending on their stoichiometries, crystalline structure and density of defects (Zheng et al., 2011; Sun et al., 2019). Tungsten trioxide (WO_3) is the most popular semiconductor among all tungsten oxides because of its exceptional chromic properties and mixed polymorphs, which manifest in rich and diverse structures (Girish Kumar and Koteswara Rao, 2015; Yin and Asakura, 2019;

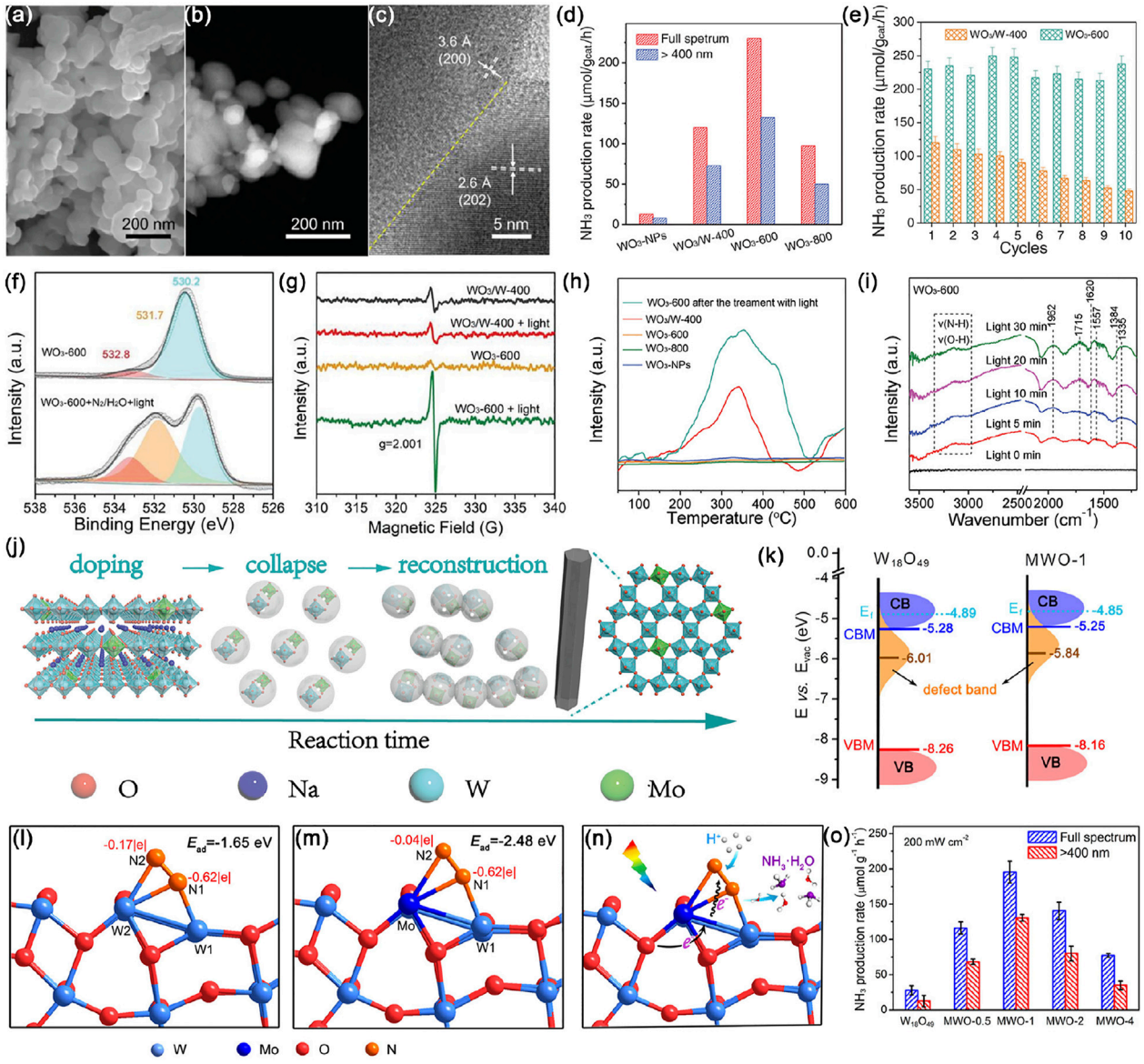

FIGURE 5
(A) Scanning electron microscopy (SEM) image, **(B)** high-angle annular dark-field scanning transmission electron microscopy (HAADF-STEM) image, and **(C)** high-resolution TEM (HRTEM) image of WO_3-600. **(D)** Photocatalytic NH_3 production rates over WO_3-NPs, WO_3/W-400, WO_3-600, and WO_3-800. **(E)** NH_3 production rates for WO_3-600 and WO_3/W-400 over the course of ten rounds of successive reactions. **(F)** Quasi *in situ* XPS spectra of O 1s in WO_3-600 before and after treatment. **(G)** *In situ* ESR spectra of WO_3/W-400 and WO_3-600 before and after light irradiation. **(H)** N_2-TPD profiles of WO_3/W-400, WO_3-600, WO_3-800, WO_3-NPs, and WO_3-600 after the treatment with light. **(I)** *In situ* DRIFT spectra recorded during the photocatalytic N_2 fixation over WO_3-600. Reproduced from Hou et al. (2019) with permission from the John Wiley and Sons. **(J)** Schematic illustration of the generation of Mo doped h-WO_3 crystalline nanowires. Reproduced from Mao et al. (2020) with permission from the John Wiley and Sons. **(K)** Schematic illustration of the electronic band structures of $W_{18}O_{49}$ and 1 mol% Mo-doped $W_{18}O_{49}$ ultrathin nanowires. Optimized adsorption configurations of N_2 molecules and their corresponding charge distribution on the surface of **(L)** $W_{18}O_{49}$ and **(M)** Mo-doped $W_{18}O_{49}$. **(N)** Scheme for photocatalytic N_2 reduction over Mo-doped $W_{18}O_{49}$. **(O)** Photocatalytic ammonia production rates by $W_{18}O_{49}$, MWO-0.5, MWO-1, MWO-2, and MWO-4 UTNWs in the first 2 h. Reproduced from Ning Zhang et al. (2018) with permission from American Chemical Society.

Cheng and Zhang, 2020). Among different structures of WO_3, the monoclinic phase is a preferred photocatalyst with the most relatively thermodynamically stable configuration than orthorhombic and hexagonal phases, while triclinic and cubic crystal structures rarely get attention (Zheng et al., 2011; Girish Kumar and Koteswara Rao, 2015; Fan et al., 2021). Hou *et al.* (Hou et al., 2019) developed a facile method to prepare monoclinic WO_3 via thermal treatment of nanoporous metals,

wherein nanoporous WO_3-600 was composed of connected grains rather than a single grain, containing abundant grain boundaries (GBs) (Figures 5A–C). Impressively, WO_3-600 showed excellent performance for photocatalytic NRR with an NH_3 yield rate as high as 230 μmol $g_{cat.}^{-1}$ h^{-1} without any sacrificial agents at room temperature, 17 times higher than that for WO_3 nanoparticles (WO_3-NPs) without GBs (Figure 5D). Moreover, almost 100% of initial activity was maintained even after ten successive reaction rounds over WO_3-600 (Figure 5E). Quasi *in situ* XPS and *in situ* electron spin resonance (ESR) measurements have been employed to verify the pivotal role of GBs in inducing a large number of operando OVs under light irradiation (Figures 5F,G). These operando OVs served as highly active sites for efficient adsorption and activation of N_2, which have been confirmed by temperature-programmed desorption of N_2 (N_2-TPD) (Figure 5H), directly contributing to easier delivery of photoexcited electrons to adsorbates through metal-oxygen covalency. Then N_2H^* intermediates coupled with protons were observed by *in situ* diffuse reflectance infrared Fourier transform (DRIFT) (Figure 5I). As shown in Figure 5J, sub-5-nm-sized nanowires of hexagonal tungsten oxide (*h*-W O $_3$) via a dopant replacement-driven molten salt method also turned out to be excellent photocatalysts with a high NH_3 production rate of 370 μmol g^{-1} h^{-1}, benefiting from unique features of the Mo-doped ultrathin hexagonal structure, thus facilitating carrier separation and dissociation of N_2 molecules (Mao et al., 2020). Tailoring the morphology of WO_3 is not only a rational route to investigate the relationship between the microstructure and photocatalytic performances, but also a feasible approach for fabricating highly photoactive nanomaterials.

Since the lattice of WO_3 withstands a considerable loss of oxygen content, the resulting nonstoichiometric tungsten suboxides (WO_{3-x}) compositions such as $W_{20}O_{58}$, $W_{18}O_{49}$ and $W_{24}O_{68}$, have suitable bandgap energy, and tunable electronic band structure, charge redistribution, as well as existence of mixed-valence W ions benefiting different degrees of oxygen deficiency in their structures (Song et al., 2015; Sun et al., 2019; Yin and Asakura, 2019; Meng Yang et al., 2020). To accommodate the large energy band of N_2, Zhang et al. (Congmin Zhang et al., 2018) used a solvothermal method to fabricate defect-rich $W_{18}O_{49}$ ultrathin nanowires doped with Mo, where Mo dopants shifted defect-band center up toward the Fermi level (E_F), thereby harvesting more photon energy to provide adequate energetic electrons for N_2 reduction (Figure 5K). Moreover, the Mo–O covalent bond facilitated the separation and transfer of photogenerated charges from coordinatively unsaturated Mo sites to N_2 adsorbates, while the formation of the Mo–W bond can effectively enhance the molecular polarization of chemisorbed N_2 as a reactive dual-active center, resulting in better activation (Figures 5L, N). The as-prepared 1 mol% Mo-doped $W_{18}O_{49}$ sample showed enhanced photocatalytic performance with an NH_3 generation rate of 195.5 μmol g^{-1} h^{-1} and STA efficiency of 0.028% under simulated sunlight (Figure 5O). Analogously, Mn^{2+} ions were introduced to replace W sites in the $W_{18}O_{49}$ lattice, which not only acted as chemisorption and activation centers for N_2 and H_2O molecules, but also facilitated the separation and migration of photogenerated charges (Ying et al., 2019). Tailoring surface oxygen vacancies and doping of tungsten oxides with heteroatoms are effective strategies to increase the number of active sites for N_2 chemisorption (Mingli Zhang et al., 2020).

3.1.2 Molybdenum trioxides

Molybdenum in the same transition metal group with tungsten shares some similar chemical properties, where a non-stoichiometric form MoO_{3-x}, analogous to WO_{3-x}, exhibits prodigious potential for solar-driven photocatalysis due to its strong OVs-induced localized surface plasmon resonance (LSPR) absorption in visible-near infrared (vis-NIR) region (Yehuan Li et al., 2019; Zheng Wang et al., 2019; Qiu et al., 2021; Li et al., 2022b). Bai *et al.* (Bai et al., 2022) synthesized Schottky-barrier-free MoO_{3-x} spheres via a facile aerosol-spray method for plasmon-driven photochemical N_2 fixation to NH_3, which features metal-like free charge carriers with the Fermi level above the bottom of the defect band and the defect band located closely to the conduction band (Figures 6A,B). The MoO_{3-x} spheres treated at 350 °C delivered an NH_3 production rate of 435.57 μmol h^{-1} g^{-1} in 20 vol% methanol aqueous solution under full-spectrum Xe lamp illumination, with an AQE of 1.24% at 808 nm and 1.12% at 1,064 nm and a STA efficiency of 0.057% in pure water under simulated sunlight (Figures 6C,D). Both the measured AQEs and the corresponding wavelengths under NIR region are among the highest values to date. Specifically, the OVs enable a perfect functional combination of rich active sites for N_2 absorption with broad-spectrum plasmon-induced hot electrons and empty states in the defect band within the MoO_{3-x} spheres, which facilitates the multi-electron reduction-oxidation (red-ox) reactions involved in photocatalytic N_2 reduction. With the Schottky-barrier-free characteristic, the hot electrons moved freely in the defect-induced electronic states and the conduction band reduced those adsorbed and activated N_2 molecules trapped at the OVs to produce NH_3, as illustrated in Figure 6B. The defective MoO_{3-x} has been exploited as matrix support to valorize rare earth La single-atom catalysts (SACs) via simple Lewis acid-base interactions due to their well-defined surface structure and high degree of anisotropy (Liu et al., 2022). The density functional theory (DFT) calculations revealed that a La single atom theoretically tends to occupy terminal OVs and coordinate with 2-coordinated O site (Mo–O–Mo, O_{2c}) to form O_{2c}-La-O_{2c} coordination. Moreover, the role of La atoms on O_{2c}–La–O_{2c} site was further clarified, which pumps energetic electrons from their unsaturated 5*d* orbitals into the π^* 2*p* orbital of the adsorbed N_2, boosting N_2 adsorption and activation. Isolated atomically dispersed La atoms anchored on MoO_{3-x}

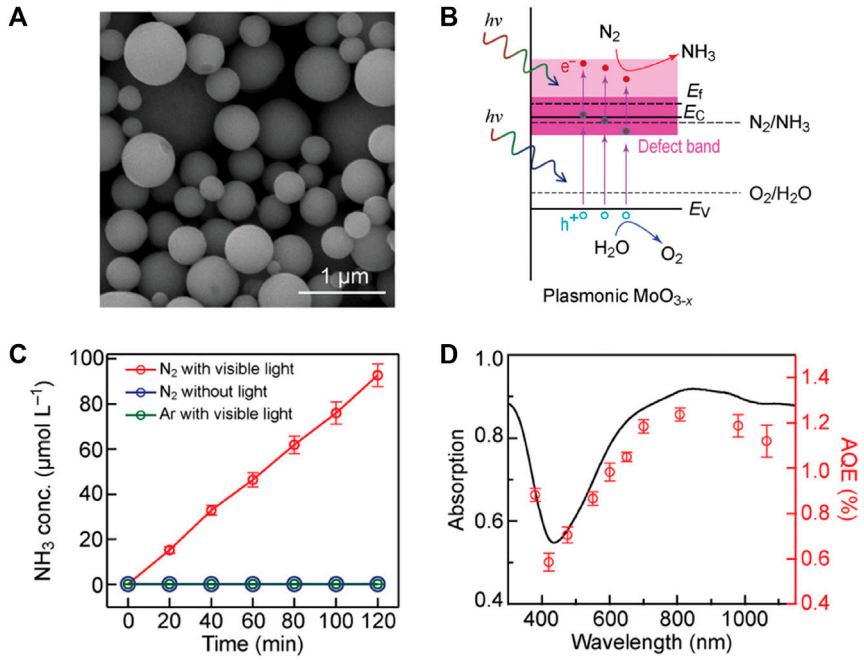

FIGURE 6
(A) SEM image of the MoO_{3-x} spheres prepared at 350°C. **(B)** Schematics illustrating the band structures of the plasmonic MoO_{3-x} photocatalyst. **(C)** Photocatalytic NH_3 production under different conditions and **(D)** AQE at different wavelengths over the MoO_{3-x} spheres. The light absorption spectrum is plotted for comparison. Reproduced from Bai et al. (2022) with permission from the John Wiley and Sons.

support were observed by the aberration-corrected HAADF-STEM and corresponding rainbow-colored images. The O_{2c}–La–O_{2c} configuration close to two oxygen coordination environment was further verified by X-ray absorption fine structure (XAFS), by which La–La bond cannot be distinctly observed in La/MoO_{3-x}. La/MoO_{3-x} possess an NH_3 production rate of 209.0 μmol h^{-1} g^{-1} without any hole scavenger under visible light, nearly 10 times that of the support. Enhanced adsorption of nitrogen and the symmetric alternative pathway following a side-on bridging adsorption configuration have been corroborated by *in situ* FT-IR spectra with the combination of DFT calculations, thus La single atoms substantially amplify the activation of N_2 toward successive hydrogenation, while lowering the formation energy barrier for *NNH → *NHNH process.

3.1.3 Mixed valence cobalt oxides

Cobalt, one of the earth-abundant first row transition metals, has gained tremendous attention for photocatalytic N_2 reduction and conversion due to its eligibility for N_2 dissociation and tunable activity (Chu et al., 2019; Gao et al., 2019), whereas its oxides with mixed-valence states of Co species have poor photostability due to photo-corrosion arising from half oxidation reaction. Combination of CoO_x with 2D carbon material supports have been rationally explored to optimize their electronic structures and tailor the active site density (Ahmed et al., 2019; Chu et al., 2019; Zhi-Yuan Wang et al., 2020; Lu et al., 2022). For example, Liu *et al.* (Yuxin Liu et al., 2021) fabricated CoO_x quantum dots anchored on porous graphdiyne (GDY) (GDY@CoO_xQD) to construct highly efficient and robust catalysts via a facile *in-situ* growth strategy for photocatalytic NRR. The composite photocatalysts featured with superlative activity and stability under various conditions as a result of strong quantum effect and a highly compatible synergistic effect. The three-dimensional configurations of the self-supported GDY@CoO_xQD nanosheet array and uniformly dispersed CoO_xQD on the porous GDY surface were confirmed by SEM and HRTEM, respectively. An average NH_3 yield rate of 46 independent experiments over the GDY@CoO_xQD in 0.1 M Na_2SO_4 aqueous solution (pH 7) up to 19,583 μmol g^{-1} h^{-1} was attained, exceeding most reported catalysts. Equally importantly, the six different batches exhibited long-term stability of 10 h with nearly constant NH_3 yield rates. By comparing the Co XPS results of CoO_xQDs on different supported carbon materials and the XANES of GDY@CoO_xQD before and after the reaction, it was concluded that the mixed-valence states of Co (Co^{3+} and Co^{2+}) played a pivotal role in enhancing the reaction activity.

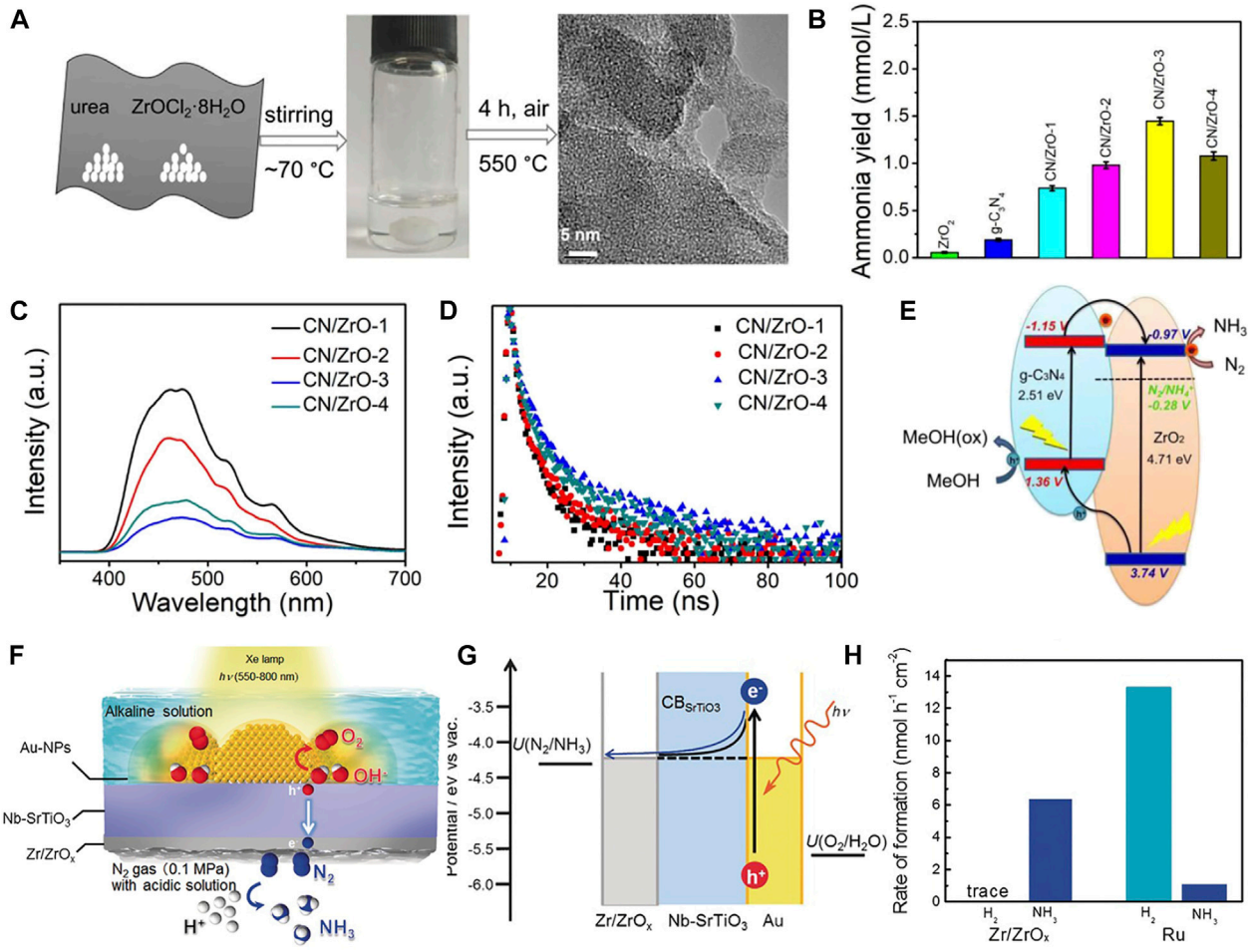

FIGURE 7
(A) Schematic of g-C_3N_4/ZrO_2 composite synthesis. **(B)** NH_3 yields of pure ZrO_2, g-C_3N_4 and g-C_3N_4/ZrO_2 composites with different ZrO_2 contents. **(C)** Photoluminescence (PL) spectroscopy and **(D)** time-resolved PL (TRPL) decay spectra. **(E)** Schematic of mechanism for photocatalytic N_2 fixation over g-C_3N_4/ZrO_2 composites. Reproduced from Mou et al. (2019) with permission from American Chemical Society. **(F)** Schematic of NRR on Au-NPs/Nb-$SrTiO_3$/Zr/ZrO_x photoelectrode. **(G)** Energy-level diagram of the plasmon-induced NH_3 synthesis device. *U*: redox potential. **(H)** NH_3 formation rate over Au-NPs/Nb-$SrTiO_3$/Zr/ZrO_x and Au-NPs/Nb-$SrTiO_3$/Ru. Reproduced from Oshikiri et al. (2016) with permission from the John Wiley and Sons.

As revealed by the DFT calculations, the introduction of GDY and the coexistence of Co^{2+}/Co^{3+} could facilitate the electron transfer to form a strong d-π^* (unocc) antibonding orbital interaction above E_F and d-π^* (occ) bonding orbital interaction below E_F. This is beneficial for weakening the bond order and bond strength of N≡N bond.

Lu et al. (2022) also reported that different cobalt oxide species were responsible for innate active properties, resulting in a synergistic effect on the two half reactions with reduction and oxidation spatially separated at CoO and Co_3O_4, respectively. The CoO-Co_3O_4 mixed-oxide (CoO dominated) composites on reduced graphene oxide (RGO) manifested a remarkable NH_3 formation efficiency of 89.1 μmol g^{-1} h^{-1}, over 14 times that of each single component. Furthermore, the photoreaction-induced cation oxidation (CoO to Co_3O_4) was reduceable/recyclable by photo-reactivating the non-active Co_3O_4 back to the active CoO at room temperature, thus leading to well-maintained NRR activity after six cycles of operation. As indicated by XANES, XPS, and HRTEM measurements, the compositions were completely transformed into Co_3O_4 during the 8 h of NRR and converted back to dominant CoO after the reactivation. The component CoO in the composite entailed deep-red-light absorbing defect states, which hindered carrier recombination. The band structure of CoO/Co_3O_4 formed a direct Z-scheme heterojunction, in

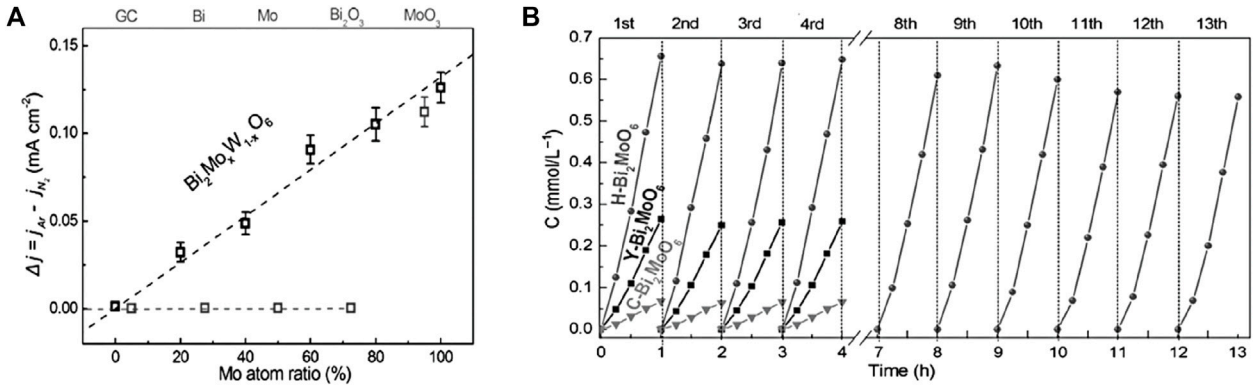

FIGURE 8
(A) The relative current densities ($\Delta j = j_{Ar} - j_{N2}$) measured at 0.6 V vs. saturated calomel electrode (SCE) of different samples. **(B)** Multicycle photocatalytic NH_3 generation from air of different samples under simulated sunlight irradiation. Reproduced from Zhao et al., 2016 with permission from the John Wiley and Sons.

which the electrons at the CB of CoO reduced N_2 molecules and the holes at the VB and defect energy levels of Co_3O_4 oxidized H_2O molecules.

3.1.4 Other transition metal oxides

Non-noble metal oxides have gained tremendous expectations as promising alternative NRR catalysts primarily owing to their high chemical stability, ease of synthesis, and minimization of noble metals consumption (Liang Yang et al., 2020; Gao et al., 2022; Zhen Zhao et al., 2022). Only a few metal oxides such as VO_2 (Haiguang Zhang et al., 2019), Ta_2O_5 (Fu et al., 2019), Nb_2O_5 (Han et al., 2018; Kong et al., 2019), NbO_2 (Huang et al., 2019), and ZrO_2 (Xu et al., 2020) have been reported for electrocatalytic NRR, However, these metal oxides suffer from large band gap, poor light absorption capacity toward visible light, low quantum efficiency, and fast recombination rate of photogenerated excitons, restricting their applications in photocatalytic NRR. The insulating material ZrO_2 with a band gap of ~5.0 eV (Xu and Schoonen, 2000) can absorb ultrahigh UV light (Gaggero et al., 2021). In addition, it possesses high mechanical strength, non-toxicity, and corrosion resistance. Intensive research has been concentrated on engineering and visible photosensitization of high band gap oxides based on Zr elements of the fourth subgroup (Oshikiri et al., 2016; Caiting Feng et al., 2022). Theoretical calculations revealed that the adsorption energy of N (ΔN^*) is much lower than that of H on the ZrO_2 surface in the aqueous photocatalytic NRR process. This suggests that ZrO_2 preferentially adsorbs N atoms and baffles the reduction of H_2O to H_2 (Skúlason et al., 2012; Tao et al., 2019). Mou *et al.* (Mou et al., 2019) demonstrated photocatalytic NRR to NH_3 based on amorphous ZrO_2 in association with *g*-C_3N_4 as a visible light harvester. The *g*-C_3N_4/ZrO_2 lamellar composites were constructed by a simple one-step pyrolysis of the deep eutectic solvent $ZrOCl_2{\cdot}8H_2O$/urea (Figure 7A). The composites imparted an optimal NH_3 yield rate of 1,446 μmol L^{-1} h^{-1} under visible light illumination, noticeably outperforming each individual counterpart (Figure 7B). The introduction of amorphous ZrO_2 restrained the hydrogen generation and facilitated N_2 reduction. A synergy between amorphous ZrO_2 and *g*-C_3N_4 was created contributing to the rapid photoproduced electron–hole pair separation and transfer (Figures 7C–E). ^{15}N isotope analysis verified the contamination-free N_2 photofixation in this work. Similarly, Oshikiri and co-workers designed a multi-component photocatalytic system of Au-NPs/Nb-$SrTiO_3$/Zr/ZrO_x. The composite was shown to have high affinity to NH_3. Plasmonic-induced charge separation happened at the Au/$SrTiO_3$ interface, thereby allowing occurrence of oxidation reactions on gold nanocrystals and N_2 reduction on the ZrO_x@Zr coating (Figures 7F,G). Figure 7H shows the large interface of ZrO_x@Zr and Nb-$SrTiO_3$ affording high selectivity and efficiency for NH_3 synthesis owing to the advantage of a stronger binding of ZrO_x@Zr to N atoms relative to H atoms compared to Ru.

3.2 Oxometallate-based photocatalysts

3.2.1 Bismuth-based oxometallates

Among various polyoxometalates, bismuth-based compounds such as Bi_2WO_6, Bi_2MoO_6 of Aurivillius structure, and $BiVO_4$ of Scheelite structure, are another class of oxides of interest because of their considerable chemical stability, up-shifted VB resulting from hybridization between Bi 6*s* and O 2*p* states and narrow band gaps,

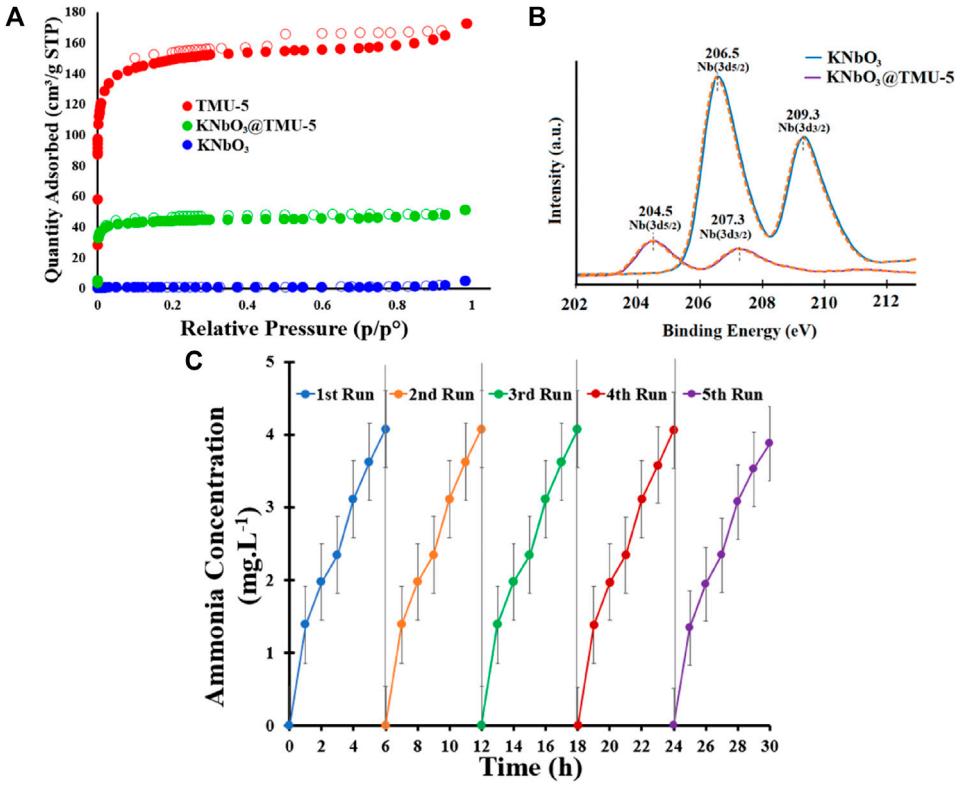

FIGURE 9
(A) N_2 adsorption/desorption isotherms for the $KNbO_3$@TMU-5 composite and its components. **(B)** Core-level XPS scans of Nb atoms of $KNbO_3$ and $KNbO_3$@TMU-5. **(C)** NH_3 concentration versus cycling test on $KNbO_3$@TMU-5. Reproduced from Chamack et al. (2022) with permission from American Chemical Society.

together with their similar layered crystal structures complimentary for charge separation and transfer (Zhang et al., 2011; Hao et al., 2020; Wenjie Liu et al., 2020; Utomo et al., 2022). Besides, the hybridization of Bi 6*s* and O 2*p* levels accounts for their largely dispersed VB, benefiting the migration of photoinduced holes and thus improving the oxidative reactions (Huang et al., 2020). Bi_2WO_6 consists of accumulated layers of discontinuous $[Bi_2O_2]^{2+}$ and octahedral $[WO_4]^{2-}$ sheets, and Bi_2MoO_6 is composed of $[MoO_2]^{2+}$ layers and $[Bi_2O_2]^{2+}$ layers, while $BiVO_4$ features with a monoclinic crystal system comprising BiO_8 and VO_4 groups (Cooper et al., 2014; Dai et al., 2016; Zhu et al., 2022). Nevertheless, the potentially high NRR activities are profoundly impeded by their intrinsic shortcomings, such as the photo-corrosion susceptibility for Bi_2WO_6, the limited light absorption in the ultraviolet region for Bi_2MoO_6, the poor water oxidation kinetics and slow mobility of photo-excited charge carriers for $BiVO_4$ (Girish Kumar and Koteswara Rao, 2015; Xin Liu et al., 2020). Also, they suffer from limited interaction with nitrogen and weak reducing ability as the CB is not sufficiently negative (Hao et al., 2020). To alleviate these problems, heteroatom doping (Meng et al., 2019; Lin Liu et al., 2021), control of facet exposure (Zhang et al., 2021), defect engineering (Haitao Li et al., 2021; Libo Wang et al., 2021; Cai Feng et al., 2022; Guoan Wang et al., 2022), heterostructure construction (Fei et al., 2019; Shende et al., 2019; Xue et al., 2019; Vesali-Kermani et al., 2020a; Chao Liu et al., 2020; Xuerui Zhang et al., 2022), morphology modification (Ning Zhang et al., 2018; Zhou et al., 2019; Sun et al., 2020; Bao et al., 2021), and regulation of internal electric fields (Lv et al., 2018) have been employed to improve the photocatalytic efficiency of N_2-to-NH_3 conversion.

Hao et al. (2016) doped Bi_2WO_6 with different ratios of Mo, combined with exposed edge unsaturated Mo atoms as the active center for N_2 adsorption, activation and photocatalytic reduction (Figure 8A). Benefiting from exposed active sites, narrower bandgap, and ultrasmall subunits in Bi_2MoO_6 system (H-Bi_2MoO_6), N_2 molecules from air were transformed into NH_3 with an NH_3 evolution rate of 1.3 mmol g^{-1} h^{-1} under simulated sunlight illumination, ≈9.5 times higher than bare Bi_2MoO_6 (Figure 8B). In another work, Wang *et al.*

demonstrated creation of enriched surface OVs via surface-layer Br doping into Bi_2MoO_6 (BMO) which boosted photocatalytic NRR activity owing to enhanced chemisorption of N_2 molecules, enlarged surface area, improved photogenerated charge separation and transfer efficiencies (Lin Wang et al., 2022). The as-made hierarchical BMO microspheres comprised small nanosheets, in which two Br replaced one MoO_4^{2-} with OH coordination balancing the crystal structure. DFT simulation indicated that Br doping promoted the formation of surface OVs at adjacent Bi, thus inducing the fabrication of the surface/internal homojunction to enhance the photogenerated charge separation. Addition of methanol as an electron donor (eliminating holes) further accelerated the generation of NH_3 with a rate of 4.77 μmol h^{-1}. The BMO showed no decrease in photocatalytic activity after five consecutive runs, manifesting its high stability, while the low stability of BMO80 in pure water indicates photogenerated hole oxidation induced by Br loss and OV reduction. Exposing different crystal facets provides enhanced spatial separation of photogenerated electrons and holes between different crystal facets. For instance, Zhang *et al.* (Zhang et al., 2021) controlled the growth of (040) and (110) facets of single-crystal $BiVO_4$ by adjusting pH, and studied the correlation of facet ratios of $BiVO_4$ crystals with photocatalytic NRR performance. They found that the activity was linearly dependent on the ratio of exposed $S_{(040)}/S_{(110)}$. Separation of space charges was boosted by *in-situ* photo-deposition of Ag NPs and MnO_x selectively loaded on the respective (040) and (110) planes. This enabled creation of a built-in electric field (BIEF) between (040)/(110) facets. Based on the results of active sites and DFT calculations, the cycle of oxygen vacancy-V^{4+}/V^{5+} in the (040) facets was inferred to be the exact active site for photocatalytic NH_3 synthesis. V^{4+} was proposed to enhance chemisorption of N_2 while V^{5+} behaved as an electron transfer bridge, and the photogenerated electrons trapped in OVs provided driving force for NRR.

3.2.2 Polymetallic oxides

Most ternary metal oxides first used for photocatalytic nitrogen fixation are titanate or Bi-based oxide systems (Chen et al., 2018; Huang et al., 2020). Higher conversion efficiency for mingled transition metal composite oxides such as Sb_2MoO_6 (Mousavi et al., 2022), $SrMoO_4$ (Luo et al., 2019), $LaCoO_3$ (Haiguang Zhang et al., 2019), $CoFe_2O_4$ (Zheng et al., 2020), $Ni_3V_2O_8$ (Vesali-Kermani et al., 2020b), $KNbO_3$ (Xing et al., 2019; Xing et al., 2020; Chamack et al., 2022), $LiNbO_3$ (Xiazhang Li et al., 2020), have been reported compared to corresponding monometallic oxides. Most mixed metal oxides are perovskite oxide compounds with wide bandgaps (Zejian Wang et al., 2021). To overcome the large band gap issue, exotic element doping, noble metal loading, and coupling with other semiconductors can be applied to broaden the light absorption range. For instance, doping of $SrMoO_4$ with Fe simultaneously introduced defect states and Fe–Mo–O active centers acting as the active sites for N_2 adsorption, which minimized bandgaps to extend the absorption edge (Luo et al., 2019). As the doping concentration increased, the intrinsic bandgap became narrowed, enabling utilization of visible light. However, the excess doped heteroatoms could act as recombination sites for photoproduced charge carriers, as reflected that the normalized photocurrent transient decreased with that of NH_3 yield at higher doping concentrations.

Niobates have emerged as a research hotspot because of their sufficiently negative CB potential endowing photogenerated electrons with strong reducibility and their spontaneous polarization nature promoting surface charge separation (Chen et al., 2019; Chao Liu et al., 2020; Nunes et al., 2020). Chen *et al.* (2021a) demonstrated the synergy effect between Bi_2S_3 and $KTa_{0.75}Nb_{0.25}O_3$ (KTN) under simulated sunlight irradiation and the simultaneous action of light and ultrasonic irradiation. The hybrid displayed high piezo-photocatalytic performance with an NH_3 production rate reaching 581 μmol L^{-1} g^{-1} h^{-1}. All samples depended on $KTa_{0.75}Nb_{0.25}O_3$ to provide the photo/piezogenerated electrons for promoting spatial charge separation, which likely played a dominant role for nitrogen fixation. A pioneering study that coupled conventional $KNbO_3$ with photoactive MOFs was conducted by Chamack *et al.* (Chamack et al., 2022). Introduction of $([Zn(OBA)\ (BPDH)_{0.5}]_n$·1.5DMF (TMU-5) enhanced the photocatalytic performance owing to the porosity, high surface area, and higher density of negative charges on Nb sites observed by N_2 adsorption/desorption isotherms and XPS scans, respectively (Figures 9A,B). In addition, $KNbO_3$@TMU-5 also exhibited good stability during the five-cycle test (Figure 9C).

3.2.3 Polyoxometalates

Polyoxometalates (POMs) are a class of discrete inorganic polynuclear anionic molecular metal-oxo clusters composed of cations and polyoxometalate polyanions linked together by shared oxygen atoms to form closed 3-dimensional frameworks. Corner-sharing metal oxide polyhedra (MO_x, x = 4, 5, and 6) are the basic building blocks, where M usually represents V, Nb, Mo, W, and Ta in high oxidation states (Yin et al., 2018; Gu et al., 2021; Horn et al., 2021). Semiconductor-like POMs or their constituent hybrids are considered as prodigious photocatalytic materials for NRR due to the following reasons: 1) the reversible gain or loss of a specific number of electrons and diverse active sites furnishing the reversible redox capability and modifiable stability; 2) the preponderance of POMs as an electron "reservoir"; 3) the well-defined HOMO–LUMO gap contributing to oxygen (ligand)-to-metal charge transfer; 4) definite particle sizes and dimensions together with the maintenance of structural intactness (Xiao-Hong Li et al., 2019; Xin Wang et al., 2020; Gu et al., 2021; Horn et al., 2021; Yuan Feng et al., 2022). Xiao *et al.* (Xiao et al., 2018) successfully covalently bonded the polyacid cluster

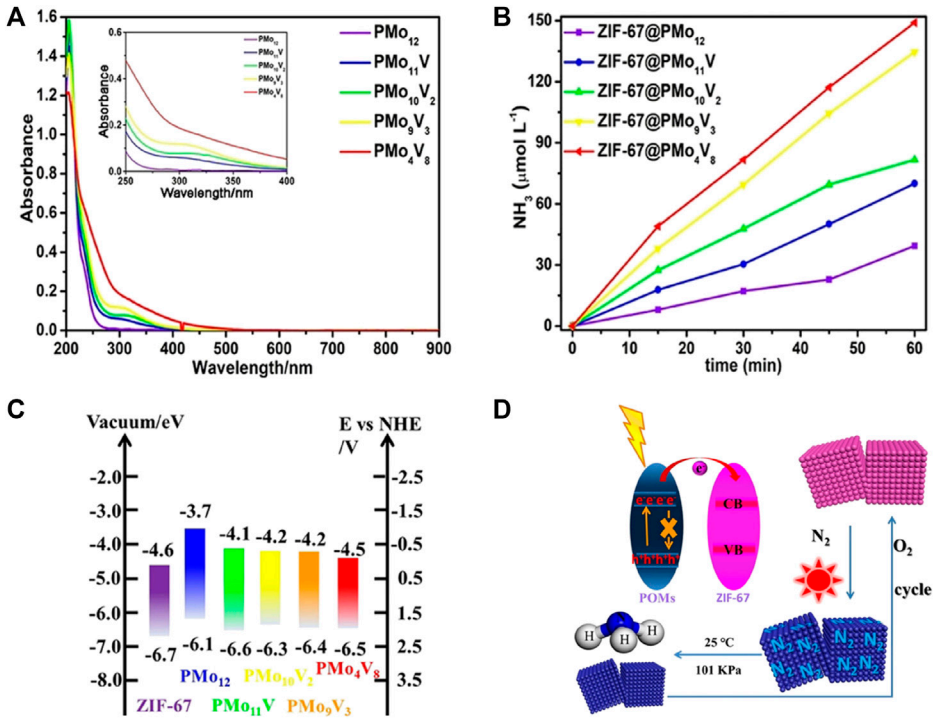

FIGURE 10
(A) UV/Vis absorption spectra of various V-substituted POMs. **(B)** NH_3 yield as a function of reaction time on various ZIF-67/POMs hybrids. **(C)** Energy levels and **(D)** electron-transfer mechanism for ZIF-67/POMs hybrids. Reproduced from Hongda Li et al. (2020) with permission from the John Wiley and Sons.

$[H_4SiO_{40}W_{12}]$ (SiW_{12}) to KOH-modified carbonitride graphite nanosheets through a phosphate bridging strategy. This allowed a rapid transfer of photogenerated electrons. The polyacid anion in POMs was suggested to function as an effective binder and electron transport chain, enhancing the interaction with the carrier and electron transport. Cyclic voltammograms of 30-SiW_{12}/K-C_3N_4 showed that a reversible two-electron redox reaction occurred at −0.06 V and −0.36 V, implying that 30-SiW_{12}/K-C_3N_4 could act as good containers of electrons and protons to provide protons for the N_2 reduction. Integration of porous zeolitic imidazolate framework-67 (ZIF-67) (to enhance N_2 adsorption) with various TM-substituted POMs ($PMo_{12-x}V_x$, x = 1, 2, 3, 8) (to supply multiple electrons), was investigated by Li *et al.* (Xiao-Hong Li et al., 2020). The light absorption of POMs was intensified to red shift by introducing V into POMs caused by the difference in the number of V hyperchromic effects (Figure 10A). The photocatalytic N_2 reduction activity increased with increasing the number of V atoms with stronger redox ability than Mo (Figure 10B). The ZIF-67/POM composites attained higher catalytic performance than that of ZIF and POMs alone with the highest N_2 fixation efficiency reaching 149.0 μmol L^{-1} h^{-1} and a STA efficiency of up to 0.032% for ZIF-67@PMo_4V_8. POMs not only improved the utilization of light energy but also easily excited electrons under light conditions to participate in the catalytic process (Figure 10C). Reduced POMs could be regenerated to form oxidized POMs in the presence of oxidants (such as O_2), enabling a complete self-healing and circulatory system (Figure 10D).

Given the solubility of POM, there are recycling problems with environmental pollution. To overcome this issue, some strategies have been developed to reinforce its stability during NRR, including adhesive (Tianyu Wang et al., 2020), coupling with MOFs (Tianyu Wang et al., 2021), and interfacial interaction (Yuan Feng et al., 2022). For example, Su et al. (2022) fabricated SiW_{12} encapsulated Cr-MOFs (MIL-101(Cr)) hybrids, which were applied to N_2 photocatalysis affording an NH_3 yield rate of 75.56 μmol h^{-1} g^{-1}, about 10 times that of $Na_4SiW_{12}O_{40}$. SiW_{12} of polyoxometalates was supposed to be the active center, which could be regulated to locate in different cavities of MIL-101(Cr) by controlling the synthesis method. This enhanced the separation efficiency of photoexcited electron-hole pairs. The N_2 reduction activity and photocatalyst structure did not change much after 5 cycles. The cooperative effect between the porous MIL-101(Cr) and SiW_{12} was hypothesized to boost the nitrogen fixation efficiency.

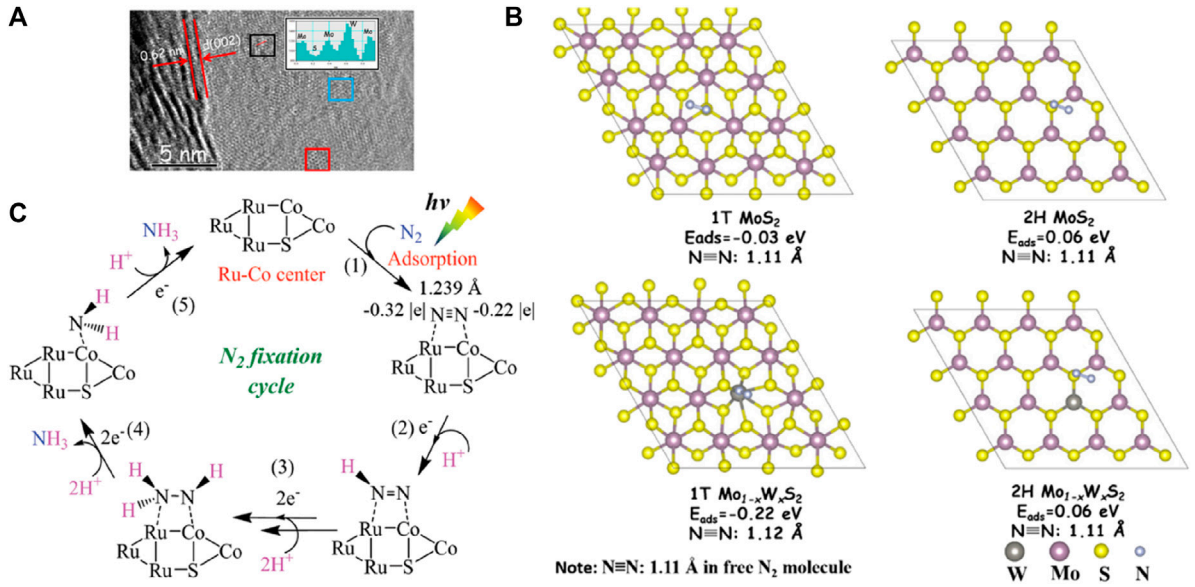

FIGURE 11
(A) HRTEM image of MWS-2 nanosheets. The red and blue squares represent the 2H and 1T structures, respectively; **(B)** Different adsorption energies of N_2 molecules on 1T MoS_2, 1T $Mo_{1-x}W_xS_2$, 2H MoS_2, and 2H $Mo_{1-x}W_xS_2$. Reproduced from Qin et al. (2021) with permission from American Chemical Society. **(C)** Proposed NRR reaction schemes on Ru-SV-CoS/CN. Reproduced from Yuan et al. (2020) with permission from the John Wiley and Sons.

3.3 Transition metal chalcogenides

Transition metal chalcogenides (TMDs) have attracted heightened research interest for photocatalytic NRR primarily owing to their outstanding optical properties (wide spectral response range), relative nontoxicity, liquid media stability, superior electronic mobility, and intrinsic catalytic activity (Sun et al., 2018; Lei et al., 2020; Shen et al., 2020; Shen et al., 2021). Sun et al. (2017) presented the trion-induced NRR on ultrathin sulfur-vacancies (SVs)-rich 2D MoS_2, where photoexcited electron-hole pairs combined the doping-induced charges to form trions, bound multiple electrons and located around the Mo sites in MoS_2, which lowered thermodynamic barriers and favored the simultaneous six-electron transfer to produce NH_3. N_2 molecules were prone to be absorbed at the SV sites and activated by the electron-rich species to form NH_3 over the SV-tuned ultrathin MoS_2. A quasi-stable NH_3 evolution rate of 325 μmol g^{-1} h^{-1} was attained without using any sacrificial agent or cocatalyst. Qin and coworkers employed a simple one-step hydrothermal method to prepare ultrathin alloyed $Mo_{1-x}W_xS_2$ nanosheets with tunable hexagonal (2H)/trigonal (1T) phase ratios using $Na_2MoO_4{\cdot}2H_2O$, $Na_2WO_4{\cdot}2H_2O$, and thiourea as Mo, W, and S precursors, respectively. Phase engineering and appropriate W doping markedly boosted the N_2 photoreduction efficiency. As shown in Figures 11A, the alloys maintained a layer structure during the hydrothermal process, and the 1T, 2H, and polymorph structural domains were also observed in the alloyed $Mo_{1-x}W_xS_2$ nanosheets. The alloyed $Mo_{1-x}W_xS_2$ nanosheets with a 1T phase concentration of 33.6% and Mo/W of 0.68:0.32 (MWS-2) were found to reach the maximal N_2 fixation rate of about 111 μmol g^{-1} h^{-1} under visible light, 3.7 (or 3)-fold higher than that of pristine MoS_2 (or WS_2). DFT calculations revealed that N_2 had the highest negative adsorption energy on 1T $Mo_{1-x}W_xS_2$ compared to that on 1T MoS_2, 2H MoS_2, and 2H $Mo_{1-x}W_xS_2$ (Figure 11B). Meanwhile, *in situ* N_2 absorption XANES techniques interpreted the energy shift on the peaks of the Mo *K*-edge as the ascending valence states of Mo, and that of W *L*-edge as a higher electron density state in W 5*d* orbitals, resulting in the migration of many electrons from Mo to W. Based on theoretical calculations and photochemical experiments, W doping and the 2H/1T structure were supposed to synergistically enhance the N_2 adsorption. Binary and ternary metal sulfide-based composites were shown to facilitate photocatalytic NH_3 synthesis via intimate heterointerfaces to diminish charge recombination (Dong Liu et al., 2021). Reported systems in this regard include MoS_2/C-ZnO (Xing et al., 2018), $C_3N_4/MoS_2/Mn_3O_4$ (Gui Li et al., 2021), WS_2@TiO_2 (Shi et al., 2020b), and MoS_2/$MgIn_2S_4$ (Swain et al., 2020).

Sparked by the nitrogenase MoFe-based protein, the reduction of N_2 on Fe single-atom-modified MoS_2 nanosheet photocatalyst was first theoretically predicted by Azofra *et al.*

(Azofra et al., 2017). Following this, various photocatalyst systems entailing Fe supported on MoS_2 have emerged. As an example, Zheng *et al.* (Zheng et al., 2021) developed Fe-decorated 2D MoS_2 photocatalysts [Fe-S_2-Mo] mimicking FeMoco in nature for NH_3 synthesis. A solar-to-NH_3 energy-conversion efficiency of 0.24% at 270°C was achieved, representing the highest efficiency among all reported photocatalytic systems thus far. The HAADF-STEM images and simulation results jointly supported that Fe atoms were favorably situated on the atop sites of Mo rather than substituted Mo sites to form inorganic Fe-S_2-Mo motifs analogous [Fe–S_2–Mo] unit in FeMoco. Theoretical calculations suggested that the HOMO and LUMO orbitals were concentrated on the edge of single-layered MoS_2 ($sMoS_2$) with relatively low electron delocalization, indicating the active edge sites of $sMoS_2$. Fe doping distinctly improved their LUMO orbital delocalization degree. Further *in situ* attenuated total reflection FTIR and the energy plots revealed that the NRR on Fe_1 over [Fe–S_2–Mo] followed an alternating pathway, showing similarity for both non-biological and biological processes regarding NRR mechanism. Excited electrons could be transferred from the VB to the CB of $sMoS_2$ via the conductive Fe–S_2–Mo motifs and reside on the Fe atom during the photoexcitation process to enter into the anti-bonding orbital of an adsorbed N_2 molecule, which thus facilitated the hydrogenation reaction of N_2 for ammonia production. Similarly, a biomimetic "MoFe cofactor" (the Fe^{3+}/Fe^{2+} and Mo^{6+}/Mo^{4+} redox couples) was introduced in $MoTe_2$ nanosheets to facilitate the transport and separation of photo-generated charge carriers by one-electron and two-electron redox reactions with 15 times longer photocarrier lifetime after Fe doping and about 11 times higher NH_3 production rate of Fe-doped $MoTe_2$ than that of pure $MoTe_2$ (Hongda Li et al., 2020). An enzymatic-analogous N_2-fixation mechanism was also demonstrated on a bimetallic Ru–Co center at Ru/CoS_x interface on *g*-C_3N_4 sheets by Ru deposition near CoS_x induced by S vacancies (Figure 11C). The side-on bridging of N_2 on under-coordinated Ru–Co center at Ru/CoS_x interface led to high polarization and strong activation of N_2, resulting in an AQE of 1.28% at 400 nm and a STA efficiency of 0.042% for NH_3 production in pure water.

3.4 Biomimetic photocatalysts

Biological nitrogen fixation has advantages of low energy consumption and high NH_3 yield, while multiple adenosine 5′-triphosphate (ATP) hydrolysis electron transfer steps are required per reduced N_2 molecule, resulting in modest overall reaction kinetics and slow NH_3 synthesis rate. Under such circumstance, exploration of biomimetic systems of molecular analogs to simulate and optimize this process has gained a tremendous interest in scientific community (Meng et al., 2021). Taking advantage of iron molybdenum sulfide chalcogels, Kanatzidis *et al.* (Banerjee et al., 2015) proposed a nitrogen-fixing biomimetic system by replacing MoFe-based proteins, which is the active site of nitrogenase, with $Fe_2Mo_6S_8$ chalcogel interconnected through $[Sn_2S_6]^{4-}$ ligands (Figure 12A). Featuring strong visible-light-absorbing, high spatial density of active sites, and multielectron transformations, the chalcogel-based amorphous framework could effectively convert N_2 to NH_3 in aqueous media under light illumination. Although its turnover number (TON) was not appealing, this study proved that cluster compounds analogous to nitrogenase can confer cogent catalysis and better stability than nitrogenase. Brown *et al.* (Brown et al., 2016) employed CdS to photosensitize MoFe proteins by harvesting light energy to replace ATP hydrolysis to drive the enzymatic N_2 fixation, with peak NH_3 production rates of 315 ± 55 nmol NH_3 $mg_{(MoFe\ protein)}^{-1}$ min^{-1} at a TOF of 75 min^{-1} (Figures 12B,C). N_2 reduction persisted for up to 5 h under constant illumination with a TON of 1.1×10^4 mol NH_3 $mol_{(MoFe\ protein)}^{-1}$. This study indicates that bio-nanocomposites can function as photocatalysts for solar-powered generation of NH_3 with TOF comparable to nitrogenase. Inspired by the above works, Liu *et al.* (Liu et al., 2016) designed a redox-active FeMoS–FeS–SnS chalcogel system consisting of $Fe_2Mo_6S_8(SPh)_3$ and Fe_3S_4 biomimetic clusters linked by Sn_2S_6 to reduce N_2 to NH_3 (Figure 12D). All FeMoS–M–SnS chalcogels constructed by replacing Fe_4S_4 clusters with redox-inert ions Sb^{3+}, Sn^{4+}, Zn^{2+}, exhibited effective NRR performance. FeMoS with FeS clusters was observed to strengthen NH_3 production over FeMoS alone and Fe_4S_4-only chalcogel (FeS–SnS) and provided higher efficiency than that of $[Mo_2Fe_6S_8(SPh)_3]$-containing chalcogels. Therefore, Fe was believed to be more conducive than Mo for N_2 binding (Figure 12E). The active sites in the Fe-containing sulfide clusters were considered to differ (i.e., based mainly on Fe) from that in the nitrogenase enzymes (based on both Mo and Fe). Quantitative isotope labeling and *in situ* DRIFTS corroborated the origin of detected NH_3 from N_2 (Figure 12F).

3.5 Metal-organic frameworks (MOFs)

MOFs are micro-mesoporous hybrid materials composed of metal ion nodes connected with organic linkers together or clusters and organic frameworks. Similar excitation characteristics of electron-hole pairs endow MOFs and their derivatives with intriguing semiconductor-like properties in various photochemical reactions (Hu et al., 2022). High microporosity and diverse functionalities enable the introduction of defined and highly exposed metal nodes onto the larger surfaces to promote or catalyze targeted reactions (Hao et al., 2021; Lin Wang et al., 2022). Especially, these exposed coordinatively unsaturated metal sites not only contribute to higher catalytic activities, but also behave as Lewis acid sites to

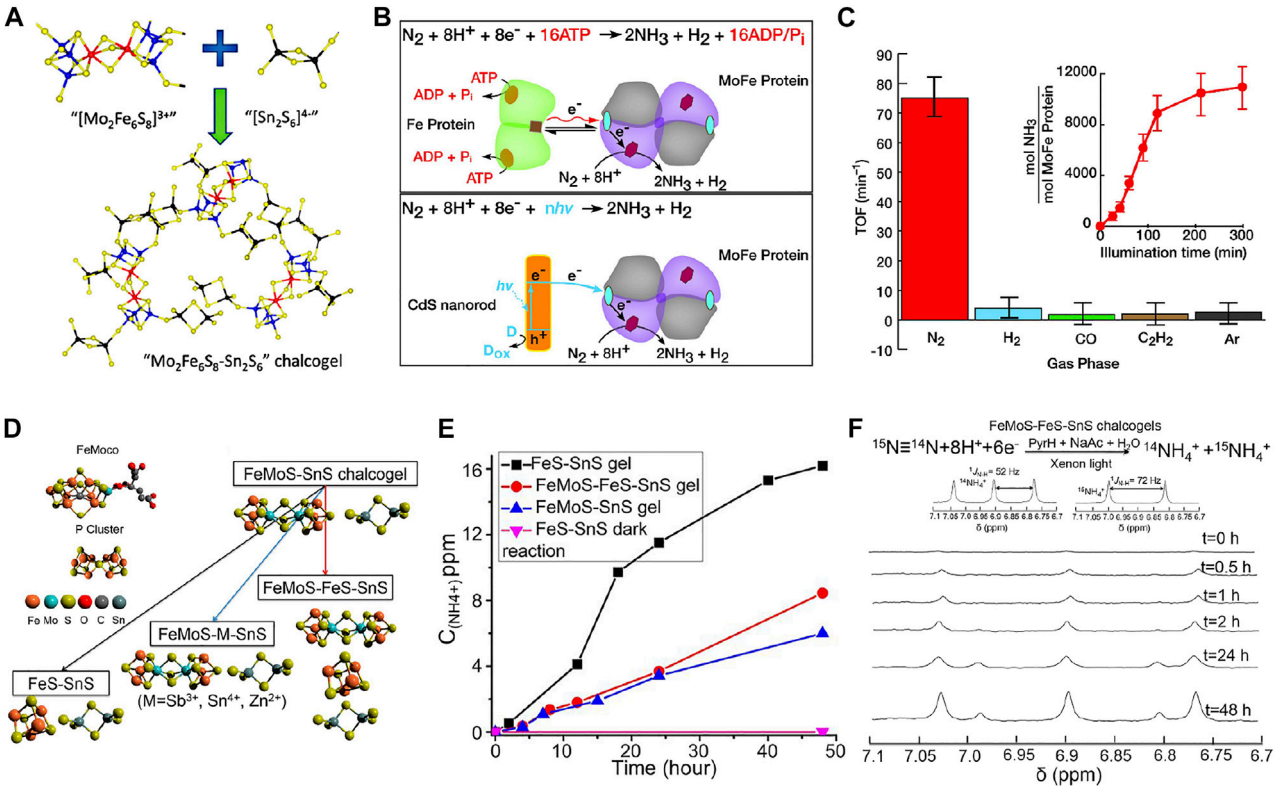

FIGURE 12
(A) Schematic of synthesis of $Mo_2Fe_6S_8$–Sn_2S_6 biomimetic chalcogel (FeMoS-chalcogel) (Mo in blue; Fe in red; S in yellow; Sn in black). Reproduced from Banerjee et al. (2015) with permission from American Chemical Society. **(B)** Reaction scheme for photocatalytic NRR to NH_3 by nitrogenase (top) and the CdS:MoFe protein biohybrids (below). **(C)** Photocatalytic NRR to NH_3 on CdS:MoFe protein biohybrids under a 100% N_2 atmosphere, 10% of either H_2, CO, or C_2H_2 in a bulk phase of 90% N_2. Reproduced from Brown et al. (2016) with permission from American Association for the Advancement of Science. **(D)** Model structures of the FeMo cofactor and P cluster, and the synthetic routes towards the assembly of different chalcogels. **(E)** Comparisons of photocatalytic NRR performance for different biomimetic chalcogels. **(F)** Isotope labeling experiment results detected by NMR. Reproduced from Liu et al. (2016) with permission from National Academy of Sciences of the United States of America.

withdraw *p* electrons from N_2 molecules and weaken the N≡N triple-bonds, accounting for photochemical N_2 reduction (Fu et al., 2022). Chen *et al.* (2021b) exploited gas-permeable MOF substrates (i.e., UiO-66) to not only serve as a stable matrix to confine the surface-clean gold nanoparticles (AuNPs) with high dispersity, but also ensure the accessibility of these AuNPs to both N_2 molecules and (hydrated) protons (Figure 13A), enabling direct plasmonic NRR with high efficiency. The porosity of the MOF matrix facilitated mass transport of reactants and products, promoting the total reaction rate (Chen et al., 2022; Guanhua Zhang et al., 2022). Accordingly, the NH_3 evolution rates on porous Au@MOFs particles were superior to those of nonporous particles at the specially designed gas–membrane–solution (GMS) reaction interface, and the GMS system was better than the powder-in-solution (PiS) system (Figure 13B). In another work, Guo *et al.* (Guo et al., 2022) investigated the $[Zr_6O_6]$ cluster effect and the leading role of photoelectrons over the protonation of nitrogen by using an N-free dehydrated Zr-based MOF, UiO-66$(SH)_2$ (Figure 13C). The UV/Vis diffuse reflectance spectrum combined with theory studies suggested that the introduction of thiol groups (–SH) caused an absorption edge of UiO-66$(SH)_2$ deep into the visible region. The hopping process of the photoelectron from VB to the unoccupied Zr-4*d*ays is dominated by the ligand-to-metal charge transfer (LMCT) (Figure 13D). The dehydration opened a "gate" for the entry of N_2 molecules into the $[Zr_6O_6]$ cluster, of which three active cage modes strongly bound with N_2 molecules and drive the cleavage of N≡N bond by the photoelectrons (Figure 13E). However, most MOF-related photocatalysts focused either on the coordination environment around the metal nodes, or the role of photosensitive ligands or single transition metals (Hu et al., 2022). Gao and co-authors presented photo-excited cluster defects and linker defects to revamp the photocatalytic NRR performance of UiO-66 (Gao et al., 2021). They shows the performance under alternate UV-Vis and visible light irradiation and after subsequent post-

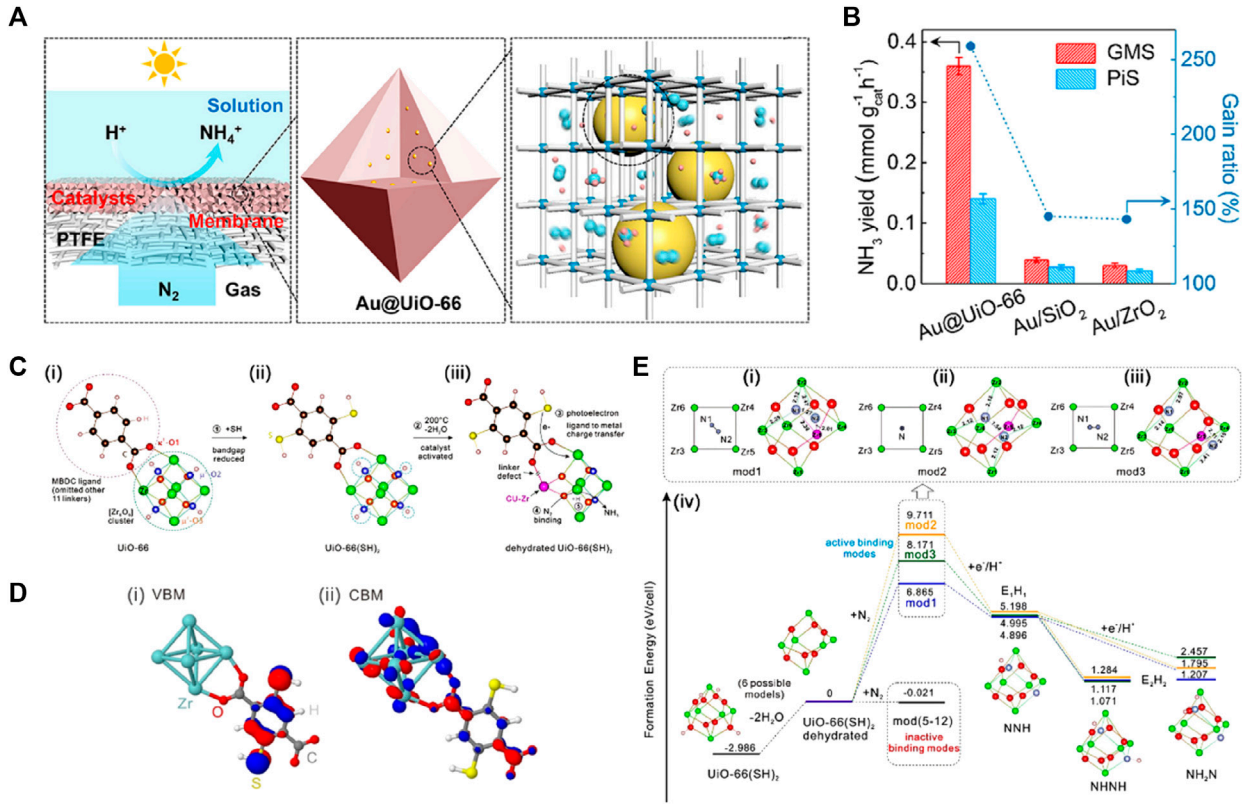

FIGURE 13
(A) Schematic illustration for direct NRR on Au encapsulated in UiO-66 matrix. **(B)** NH_3 yield on powder (in the PiS system) and membrane (in the GMS system) catalysts consisting of Au@UiO-66, Au/SiO_2, and Au/ZrO_2. Reproduced from Chen et al. (2021b) with permission from American Chemical Society. **(C)** Schematic evolution of the partial structure of UiO66, UiO-66(SH)$_2$ and the dehydrated UiO-66(SH)$_2$. **(D)** The calculated band orbitals for VBM and CBM of UiO-66(SH)$_2$ at Γ point. **(E)** The three active modes (mod 1–3) with each centerpiece configuration of the [Zr_6O_6] cluster encaging N_2 molecule and their corresponding formation energy diagrams. Reproduced from Guo et al. (2022) with permission from the John Wiley and Sons.

synthetic ligand exchange (PSE) process. Compared to UV-Vis light, the performance of the second test under visible light did not improve. After the PSE process that repaired linker defects instead of cluster defects, activity was restored under UV-Vis light. This demonstrated that photo-induced defects can only be created by UV light, where linker defects played a critical role in improving the performance due to the Zr nodes with unsaturated coordination induced by linker defects being more conducive to photo-driven NH_3 synthesis.

Designing and constructing photocatalysts with bimetallic active centers is an effective way for nitrogen photofixation (Zhen Zhao et al., 2022). An *et al.* (An et al., 2021) designed a series of modularized UiO-66-based MOFs, U(Zr-Hf)-X, with bimetallic Zr-Hf nodes and functionalized ligands, and demonstrated a tandem ligand-to-metal-to-metal electron transfer (LMMET) pathway. By independently manipulating the Zr/Hf molar ratio and substituent group of TPA, the optimal U (0.5Hf)-2SH (metal nodes: 0.5Zr: 0.5Hf; linkers: TPA-2SH) yielded an NH_3 production rate up to 116.1 μmol h^{-1} g^{-1} under visible light. This was attributed to the broadening of the absorption spectrum to visible light by –2SH modification according to combined experiment-theory results. Although these results suggested that the synergistic effect of bimetallic Zr-Hf nodes was favorable for NRR performance, it is uncertain whether the TPA-2SH ligand contributed to charger transfer mechanism. The proposed NRR pathway of U (0.5Hf)-2SH was explored. The one-step two-photon excitation path strides across the uphill process of the electron transfer from TPA-2SH ligands to metal nodes in UiO-66. The Hf species served as an electron buffer tank to optimize the electron transfer, while the Zr species acted as the catalytic active site due to the difference in electrode potentials between Zr–O and Hf–O clusters. Meanwhile, Zr-dominated π-backbonding mechanism weakened the N≡N bond in absorbed N_2 molecules via the electron transfer synergy to generate NH_3. Nonetheless, research on photocatalytic NRR using MOFs is relatively rare, the existing MOF-based photocatalysts have still

an exemplary significance regarding constructing other visible-light-driven MOF-based NRR photocatalysts.

4 Conclusions and future remarks

The photocatalytic NRR is an appealing alternative to the current industrial thermocatalytic Haber-Bosch process for NH_3 production. It only requires solar energy and water, rendering the process environmentally friendly and highly sustainable. With a general awareness of emphasizing on green chemistry and sustainable development, this field is bound to have a significant and far-reaching impact on how humans understand and engage in the nitrogen cycle. Despite recent progresses that have been achieved in the field of photocatalytic NH_3 synthesis, it is still in its infancy. A comparable conversion efficiency to the century-old Haber-Bosch process remains unsolved, especially on how to accentuate N_2 activation and accelerate the kinetics of electron transfer to N_2. Continuous efforts in the design and development of nontoxic, efficient, stable and low-cost catalysts minimizing the consumption of noble metals have obtained some positive advancements. Tungsten and related metal-based materials have shown enormous accolades as photocatalysts for NRR. However, there still remain many challenges to be addressed as follows:

1) The intrinsic mechanism and kinetic control of nitrogen fixation are still ambiguous and complex, warranting further investigations. Because of the complex multi-electron reactions involved and the presence of various intermediate species, combination of multiple accurate analytical methods and advanced characterization techniques are required. It is essential to develop *in-situ* techniques to study the adsorption structure of N_2 and key intermediates on the surface of catalytic materials, providing useful information on the catalytic active center and its dynamic evolution during the reaction process.
2) Various environmental factors (such as cation effect, electric field effect, pH, hydrophobicity, and actual active site, *etc.*) (Zhou et al., 2022) can profoundly affect the photocatalytic NRR process. It is thus necessary to explore and clarify the synergistic effect among the semiconductor photocatalysts and mixed solvent systems to further reveal the multi-effects of collaborative catalytic mechanism.
3) Equally importantly, the cooperative mechanisms among heterostructure, element doping and interaction between components and role of each individual strategy in N_2 photocatalysis remain to be elucidated. It is necessary to comprehensively use various design and control strategies of catalysts to combine element doping, defect construction, and structural design to increase active sites, suppress the recombination of photogenerated carriers, and enhance the adsorption and activation of nitrogen molecules in the NRR process.
4) Efficient utilization of solar energy is the focus of interest in photocatalysis. However, the utilization of light in the NIR and the far-infrared region above 1,000 nm for NRR photocatalysis is poor. To facilitate the practical utilization of NRR photocatalysis, the design of suitable photocatalysts for wide-range light harvest from ultraviolet to near-infrared regions is important. This may be realized by integration with NIR and even far-infrared responsive materials such as dye molecules and black phosphorus (Zhang et al., 2017), narrow band gap NIR harvesters as well as materials having surface plasmon resonance effect.
5) The extensive use of sacrificial agents leads to additional costs, which deteriorate the overall affordability of the environment. Therefore, some cheap sacrificial agents at this stage, such as starch, biomass, plastics, wastewater, *etc.*, could also be developed as sacrificial agents to further reduce the cost of large-scale application of N_2 photocatalysis.
6) The attained SCE of N_2 photoreduction is still less than 1%, far below the minimum standard of 10% needed to realize industrialization, and the stability during the reaction process is however still much below the requirements for long-term practical applications.
7) The photostability of semiconductor catalysts is another adverse issue that deserves much attention. The surfaces of many *n*-type and *p*-type semiconductors (such as sulphides) are susceptible to decomposition by photogenerated holes or electrons, decreasing the lifetimes of the photocatalysts. To address this issue, strategies such as coating with a second phase, surface passivation and functionalization and incorporation with cocatalysts can be employed (Sun et al., 2018).

To date, major endeavors in materials engineering toward N_2 photocatalysis have been made on traditional semiconductors. Some emerging photocatalytic materials such as MOFs and covalent organic frameworks (COFs) have not been fully explored for photocatalytic N_2 reduction. Meanwhile, the design of cation defects and further combined defects and investigation of their roles in MOFs in N_2 reduction are rarely conducted, which deserves further studies. To synergistically promote N_2 photocatalysis, integration of multiple design strategies (e.g., defect engineering and other modification strategies such as creation of Z-scheme heterostructures to separate ammonia production and water oxidation sites in space) is preferred. Additionally, combination of material engineering and external fields (e.g., microwaves, mechanical stress, temperature gradient, electric field, magnetic field, and coupled fields) is another promising strategy to further boost photocatalytic N_2 reduction reactions.

Current research focuses mainly on the microstructure design of materials and the improvement of photocatalytic performance, while less attention was paid on the development of photocatalytic devices suitable for future applications and reliable

cost accounting. The bridge between laboratory research and practical application development is crucial. To better understand the conditions required to reach practical industrial applications, we should compare photocatalytic NRR with current industrial Haber-Bosch reactions from various perspectives, such as reaction temperature and pressure, ammonia/nitrate output, pollution, etc. In an actual photoreactor, N_2 would be separated from the air using standard cryogenic separation or membrane processes and would need to be recovered and recycled for cost reasons. Current Photocatalytic NRR is more carried out in aqueous solutions, which means that liquid-phase products can be directly obtained to produce liquid fertilizers that can be directly used and sold, but the subsequent separation of catalysts will further increase the energy cost of the entire process. Even if the final product is anhydrous ammonia for fuel feedstock, the purification of low concentrations of NH_3 from the N_2 stream adds to the energy-consuming step. Therefore, how to achieve higher product concentrations in flowing gas setups is an important target of this particular approach. From another point of view, this idea guides us to no longer pay attention to the NH_3 yield as an indicator, but to focus on the integration of upstream synthesis and downstream applications to reduce energy consumption and pollution in the entire production process, to achieve the final goal of "carbon neutrality" faster.

Author contributions

All authors listed have made a substantial, direct, and intellectual contribution to the work and approved it for publication.

Funding

This work was supported by the National Natural Science Foundation of China (No. 21972010) and the Beijing Natural Science Foundation (No. 2192039).

Conflict of interest

The authors declare that the research was conducted in the absence of any commercial or financial relationships that could be construed as a potential conflict of interest.

Publisher's note

All claims expressed in this article are solely those of the authors and do not necessarily represent those of their affiliated organizations, or those of the publisher, the editors and the reviewers. Any product that may be evaluated in this article, or claim that may be made by its manufacturer, is not guaranteed or endorsed by the publisher.

Supplementary material

The Supplementary Material for this article can be found online at: https://www.frontiersin.org/articles/10.3389/fchem.2022.978078/full#supplementary-material

References

Ahmed, M. I., Chen, S., Ren, W., Chen, X., and Zhao, C. (2019). Synergistic bimetallic $CoFe_2O_4$ clusters supported on graphene for ambient electrocatalytic reduction of nitrogen to ammonia. *Chem. Commun.* 55 (81), 12184–12187. doi:10.1039/C9CC05684J

An, K., Ren, H., Yang, D., Zhao, Z., Gao, Y., Chen, Y., et al. (2021). Nitrogenase-inspired bimetallic metal organic frameworks for visible-light-driven nitrogen fixation. *Appl. Catal. B Environ.* 292, 120167. doi:10.1016/j.apcatb.2021.120167

Andersen, S. Z., Colic, V., Yang, S., Schwalbe, J. A., Nielander, A. C., McEnaney, J. M., et al. (2019). A rigorous electrochemical ammonia synthesis protocol with quantitative isotope measurements. *Nature* 570 (7762), 504–508. doi:10.1038/s41586-019-1260-x

Azofra, L. M., Sun, C., Cavallo, L., and MacFarlane, D. R. (2017). Feasibility of N_2 binding and reduction to ammonia on Fe-deposited MoS_2 2D sheets: A DFT study. *Chem. Eur. J.* 23 (34), 8275–8279. doi:10.1002/chem.201701113

Bai, J., Chen, X., Xi, Z. Y., Wang, X., Li, Q., Hu, S. Z., et al. (2017). Influence of solvothermal post-treatment on photochemical nitrogen conversion to ammonia with g-C_3N_4 Catalyst. *Acta Phys. -Chim. Sin.* 33 (3), 611–619. doi:10.3866/pku.Whxb201611102

Bai, H., Lam, S. H., Yang, J., Cheng, X., Li, S., Jiang, R., et al. (2022). A Schottky-barrier-free plasmonic semiconductor photocatalyst for nitrogen fixation in a "one-stone-two-birds" manner. *Adv. Mat.* 34 (2), 2104226. doi:10.1002/adma.202104226

Banerjee, A., Yuhas, B. D., Margulies, E. A., Zhang, Y., Shim, Y., Wasielewski, M. R., et al. (2015). Photochemical nitrogen conversion to ammonia in ambient conditions with FeMoS-chalcogels. *J. Am. Chem. Soc.* 137 (5), 2030–2034. doi:10.1021/ja512491v

Bao, L., Yuan, Y.-j., Zhang, H., Zhang, X., and Xu, G. (2021). Understanding the hierarchical behavior of Bi_2WO_6 with enhanced photocatalytic nitrogen fixation activity. *Dalton Trans.* 50 (21), 7427–7432. doi:10.1039/D1DT00762A

Bazhenova, T. A., and Shilov, A. E. (1995). Nitrogen fixation in solution. *Coord. Chem. Rev.* 144, 69–145. doi:10.1016/0010-8545(95)01139-G

Bo, Y., Wang, H., Lin, Y., Yang, T., Ye, R., Li, Y., et al. (2021). Altering hydrogenation pathways in photocatalytic nitrogen fixation by tuning local electronic structure of oxygen vacancy with dopant. *Angew. Chem. Int. Ed.* 60 (29), 16085–16092. doi:10.1002/anie.202104001

Brown, K. A., Harris, D. F., Wilker, M. B., Rasmussen, A., Khadka, N., Hamby, H., et al. (2016). Light-driven dinitrogen reduction catalyzed by a CdS: Nitrogenase MoFe protein biohybrid. *Science* 352 (6284), 448–450. doi:10.1126/science.aaf2091

Cai Feng, C., Wu, P., Li, Q., Liu, J., Wang, D., Liu, B., et al. (2022). Amorphization and defect engineering in constructing ternary composite $Ag/PW_{10}V_2/am\text{-}TiO_{2-x}$ for enhanced photocatalytic nitrogen fixation. *New J. Chem.* 46 (4), 1731–1740. doi:10.1039/D1NJ05917C

Caiting Feng, C., Liu, J., Li, Q., Ji, L., Wu, P., Yuan, X., et al. (2022). Fabricating $Ag/PW_{12}/Zr\text{-}mTiO_2$ composite via doping and interface engineering: An efficient catalyst with bifunctionality in photo- and electro-driven nitrogen reduction reactions. *Adv. Sustain. Syst.* 6 (1), 2100307. doi:10.1002/adsu.202100307

Cao, S., Chen, H., Jiang, F., and Wang, X. (2018). Nitrogen photofixation by ultrathin amine-functionalized graphitic carbon nitride nanosheets as a gaseous product from thermal polymerization of urea. *Appl. Catal. B Environ.* 224, 222–229. doi:10.1016/j.apcatb.2017.10.028

Chamack, M., Ifires, M., Akbar Razavi, S. A., Morsali, A., Addad, A., Larimi, A., et al. (2022). Photocatalytic performance of perovskite and metal-organic framework hybrid material for the reduction of N_2 to ammonia. *Inorg. Chem.* 61 (3), 1735–1744. doi:10.1021/acs.inorgchem.1c03622

Chao Liu, C., Zhang, Q., Hou, W., and Zou, Z. (2020). 2D titanium/niobium metal oxide-based materials for photocatalytic application. *Sol. RRL* 4 (9), 2000070. doi:10.1002/solr.202000070

Chen, W. T., Chan, A., Al-Azri, Z. H. N., Dosado, A. G., Nadeem, M. A., Sun-Waterhouse, D., et al. (2015). Effect of TiO_2 polymorph and alcohol sacrificial agent on the activity of Au/TiO_2 photocatalysts for H_2 production in alcohol–water mixtures. *J. Catal.* 329, 499–513. doi:10.1016/j.jcat.2015.06.014

Chen, X., Li, N., Kong, Z., Ong, W.-J., and Zhao, X. (2018). Photocatalytic fixation of nitrogen to ammonia: State-of-the-art advancements and future prospects. *Mat. Horiz.* 5 (1), 9–27. doi:10.1039/c7mh00557a

Chen, F., Huang, H., Guo, L., Zhang, Y., and Ma, T. (2019). The role of polarization in photocatalysis. *Angew. Chem. Int. Ed.* 58 (30), 10061–10073. doi:10.1002/anie.201901361

Chen, L., Dai, X., Li, X., Wang, J., Chen, H., Hu, X., et al. (2021a). A novel Bi_2S_3/$KTa_{0.75}Nb_{0.25}O_3$ nanocomposite with high efficiency for photocatalytic and piezocatalytic N_2 fixation. *J. Mat. Chem. A* 9 (22), 13344–13354. doi:10.1039/D1TA02270A

Chen, L., Hao, Y.-C., Guo, Y., Zhang, Q., Li, J., Gao, W.-Y., et al. (2021b). Metal-organic framework membranes encapsulating gold nanoparticles for direct plasmonic photocatalytic nitrogen fixation. *J. Am. Chem. Soc.* 143 (15), 5727–5736. doi:10.1021/jacs.0c13342

Chen, C., Sun, M., Wang, K., and Li, Y. (2022). Dual-metal single-atomic catalyst: The challenge in synthesis, characterization, and mechanistic investigation for electrocatalysis. *SmartMat.* doi:10.1002/smm2.1085

Chen-Xuan Xu, C. X., Huang, J. D., and Ma, J. M. (2021). Green, cheap and rechargeable Al–N_2 battery with efficient N_2 fixation. *Rare Met.* 40 (1), 1–2. doi:10.1007/s12598-020-01626-8

Cheng, Q., and Zhang, G.-K. (2020). Enhanced photocatalytic performance of tungsten-based photocatalysts for degradation of volatile organic compounds: A review. *Tungsten* 2 (3), 240–250. doi:10.1007/s42864-020-00055-5

Choi, J., Suryanto, B. H. R., Wang, D., Du, H. L., Hodgetts, R. Y., Ferrero Vallana, F. M., et al. (2020). Identification and elimination of false positives in electrochemical nitrogen reduction studies. *Nat. Commun.* 11 (1), 5546. doi:10.1038/s41467-020-19130-z

Chu, K., Liu, Y.-p., Li, Y.-b., Zhang, H., and Tian, Y. (2019). Efficient electrocatalytic N_2 reduction on CoO quantum dots. *J. Mat. Chem. A* 7 (9), 4389–4394. doi:10.1039/C9TA00016J

Comer, B. M., and Medford, A. J. (2018). Analysis of photocatalytic nitrogen fixation on rutile TiO_2 (110). *ACS Sustain. Chem. Eng.* 6 (4), 4648–4660. doi:10.1021/acssuschemeng.7b03652

Congmin Zhang, C., Chen, G., Lv, C., Yao, Y., Xu, Y., Jin, X., et al. (2018). Enabling nitrogen fixation on Bi_2WO_6 photocatalyst by c-PAN surface decoration. *ACS Sustain. Chem. Eng.* 6 (9), 11190–11195. doi:10.1021/acssuschemeng.8b02236

Cooper, J. K., Gul, S., Toma, F. M., Chen, L., Glans, P.-A., Guo, J., et al. (2014). Electronic structure of monoclinic $BiVO_4$. *Chem. Mat.* 26 (18), 5365–5373. doi:10.1021/cm5025074

Dai, Z., Qin, F., Zhao, H., Ding, J., Liu, Y., Chen, R., et al. (2016). Crystal defect engineering of Aurivillius Bi_2MoO_6 by Ce doping for increased reactive species production in photocatalysis. *ACS Catal.* 6 (5), 3180–3192. doi:10.1021/acscatal.6b00490

Dimitrijevic, N. M., Vijayan, B. K., Poluektov, O. G., Rajh, T., Gray, K. A., He, H., et al. (2011). Role of water and carbonates in photocatalytic transformation of CO_2 to CH_4 on titania. *J. Am. Chem. Soc.* 133 (11), 3964–3971. doi:10.1021/ja108791u

Dong Liu, D., Chen, S., Li, R., and Peng, T. (2021). Review of Z-scheme heterojunctions for photocatalytic energy conversion. *Acta Phys. -Chim. Sin.* 37 (6), 2010017. doi:10.3866/pku.Whxb202010017

Dong Zhang, D., Li, Y., Li, Y., and Zhan, S. (2022). Towards single-atom photocatalysts for future carbon-neutral application. *SmartMat.* doi:10.1002/smm2.1095

Fan, Y. S., Xi, X. L., Liu, Y. S., Nie, Z.-R., Zhao, L. Y., Zhang, Q. H., et al. (2021). Regulation of morphology and visible light-driven photocatalysis of WO_3 nanostructures by changing pH. *Rare Met.* 40 (7), 1738–1745. doi:10.1007/s12598-020-01490-6

Fei, T., Yu, L., Liu, Z., Song, Y., Xu, F., Mo, Z., et al. (2019). Graphene quantum dots modified flower like Bi_2WO_6 for enhanced photocatalytic nitrogen fixation. *J. Colloid Interface Sci.* 557, 498–505. doi:10.1016/j.jcis.2019.09.011

Feng Wang, F., Ding, Q., Bai, Y., Bai, H., Wang, S., Fan, W., et al. (2022). Fabrication of an amorphous metal oxide/p-$BiVO_4$ photocathode: Understanding the role of entropy for reducing nitrate to ammonia. *Inorg. Chem. Front.* 9 (4), 805–813. doi:10.1039/D1QI01472B

Fu, W., Zhuang, P., OliverLam Chee, M., Dong, P., Ye, M., Shen, J., et al. (2019). Oxygen vacancies in Ta_2O_5 nanorods for highly efficient electrocatalytic N_2 reduction to NH_3 under ambient conditions. *ACS Sustain. Chem. Eng.* 7 (10), 9622–9628. doi:10.1021/acssuschemeng.9b01178

Fu, Y., Liao, Y., Li, P., Li, H., Jiang, S., Huang, H., et al. (2022). Layer structured materials for ambient nitrogen fixation. *Coord. Chem. Rev.* 460, 214468. doi:10.1016/j.ccr.2022.214468

Gaggero, E., Calza, P., Cerrato, E., and Paganini, M. C. (2021). Cerium-europium- and erbium-modified ZnO and ZrO_2 for photocatalytic water treatment applications: A review. *Catalysts* 11 (12), 1520. doi:10.3390/catal11121520

Gambarotta, S., and Scott, J. (2004). Multimetallic cooperative activation of N_2. *Angew. Chem. Int. Ed.* 43 (40), 5298–5308. doi:10.1002/anie.200301669

Gao, X., Wen, Y., Qu, D., An, L., Luan, S., Jiang, W., et al. (2018). Interference effect of alcohol on Nessler's reagent in photocatalytic nitrogen fixation. *ACS Sustain. Chem. Eng.* 6 (4), 5342–5348. doi:10.1021/acssuschemeng.8b00110

Gao, Y., Han, Z., Hong, S., Wu, T., Li, X., Qiu, J., et al. (2019). ZIF-67-derived cobalt/nitrogen-doped carbon composites for efficient electrocatalytic N_2 reduction. *ACS Appl. Energy Mat.* 2 (8), 6071–6077. doi:10.1021/acsaem.9b01135

Gao, W., Li, X., Zhang, X., Su, S., Luo, S., Huang, R., et al. (2021). Photocatalytic nitrogen fixation of metal–organic frameworks (MOFs) excited by ultraviolet light: Insights into the nitrogen fixation mechanism of missing metal cluster or linker defects. *Nanoscale* 13 (16), 7801–7809. doi:10.1039/D1NR00697E

Gao, Y., Xia, Q., Hao, L., Robertson, A. W., and Sun, Z. (2022). Design of porous core–shell manganese oxides to boost electrocatalytic dinitrogen reduction. *ACS Sustain. Chem. Eng.* 10 (3), 1316–1322. doi:10.1021/acssuschemeng.1c07824

Garden, A. L., and Skúlason, E. (2015). The mechanism of industrial ammonia synthesis revisited: Calculations of the role of the associative mechanism. *J. Phys. Chem. C* 119 (47), 26554–26559. doi:10.1021/acs.jpcc.5b08508

Girish Kumar, S., and Koteswara Rao, K. S. R. (2015). Tungsten-based nanomaterials (WO_3 & Bi_2WO_6): Modifications related to charge carrier transfer mechanisms and photocatalytic applications. *Appl. Surf. Sci.* 355, 939–958. doi:10.1016/j.apsusc.2015.07.003

Gu, J., Chen, W., Shan, G. G., Li, G., Sun, C., Wang, X. L., et al. (2021). The roles of polyoxometalates in photocatalytic reduction of carbon dioxide. *Mat. Today Energy* 21, 100760. doi:10.1016/j.mtener.2021.100760

Guanhua Zhang, G., Yuan, X., Xie, B., Meng, Y., Ni, Z., Xia, S., et al. (2022). S vacancies act as a bridge to promote electron injection from Z-scheme heterojunction to nitrogen molecule for photocatalytic ammonia synthesis. *Chem. Eng. J.* 433, 133670. doi:10.1016/j.cej.2021.133670

Gui Li, G., Yang, W., Gao, S., Shen, Q., Xue, J., Chen, K., et al. (2021). Creation of rich oxygen vacancies in bismuth molybdate nanosheets to boost the photocatalytic nitrogen fixation performance under visible light illumination. *Chem. Eng. J.* 404, 127115. doi:10.1016/j.cej.2020.127115

Guo, B., Cheng, X., Tang, Y., Guo, W., Deng, S., Wu, L., et al. (2022). Dehydrated UiO-66$(SH)_2$: The Zr–O Cluster and its photocatalytic role mimicking the biological nitrogen fixation. *Angew. Chem. Int. Ed. Engl.* 61 (13), e202117244. doi:10.1002/anie.202117244

Guo, C. X., Ran, J., Vasileff, A., and Qiao, S. Z. (2018). Rational design of electrocatalysts and photo(electro)catalysts for nitrogen reduction to ammonia (NH_3) under ambient conditions. *Energy Environ. Sci.* 11 (1), 45–56. doi:10.1039/C7EE02220D

Guo, J., and Chen, P. (2017). Catalyst: NH_3 as an energy carrier. *Chem* 3 (5), 709–712. doi:10.1016/j.chempr.2017.10.004

Guoan Wang, G., Huo, T., Deng, Q., Yu, F., Xia, Y., Li, H., et al. (2022). Surface-layer bromine doping enhanced generation of surface oxygen vacancies in bismuth molybdate for efficient photocatalytic nitrogen fixation. *Appl. Catal. B Environ.* 310, 121319. doi:10.1016/j.apcatb.2022.121319

Haiguang Zhang, H., Li, X., Su, H., Chen, X., Zuo, S., Yan, X., et al. (2019). Sol–gel synthesis of upconversion perovskite/attapulgite heterostructures for photocatalytic fixation of nitrogen. *J. Sol-Gel Sci. Technol.* 92 (1), 154–162. doi:10.1007/s10971-019-05071-7

Haitao Li, H., Liu, Y., Liu, Y., Wang, L., Tang, R., Deng, P., et al. (2021). Efficient visible light driven ammonia synthesis on sandwich structured C_3N_4/MoS_2/Mn_3O_4 catalyst. *Appl. Catal. B Environ.* 281, 119476. doi:10.1016/j.apcatb.2020.119476

Han, J., Liu, Z., Ma, Y., Cui, G., Xie, F., Wang, F., et al. (2018). Ambient N_2 fixation to NH_3 at ambient conditions: Using Nb_2O_5 nanofiber as a high-performance electrocatalyst. *Nano Energy* 52, 264–270. doi:10.1016/j.nanoen.2018.07.045

Hao Li, H., Shang, J., Shi, J., Zhao, K., and Zhang, L. (2016). Facet-dependent solar ammonia synthesis of BiOCl nanosheets via a proton-assisted electron transfer pathway. *Nanoscale* 8 (4), 1986–1993. doi:10.1039/C5NR07380D

Hao, Y., Dong, X., Zhai, S., Ma, H., Wang, X., Zhang, X., et al. (2016). Hydrogenated bismuth molybdate nanoframe for efficient sunlight-driven nitrogen fixation from air. *Chem. Eur. J.* 22 (52), 18722–18728. doi:10.1002/chem.201604510

Hao, Q., Liu, C., Jia, G., Wang, Y., Arandiyan, H., Wei, W., et al. (2020). Catalytic reduction of nitrogen to produce ammonia by bismuth-based catalysts: State of the art and future prospects. *Mat. Horiz.* 7 (4), 1014–1029. doi:10.1039/C9MH01668F

Hao, L., Xia, Q., Zhang, Q., Masa, J., and Sun, Z. (2021). Improving the performance of metal-organic frameworks for thermo-catalytic CO_2 conversion: Strategies and perspectives. *Chin. J. Catal.* 42 (11), 1903–1920. doi:10.1016/S1872-2067(21)63841-X

Hinnemann, B., and Nørskov, J. K. (2006). Catalysis by enzymes: The biological ammonia synthesis. *Top. Catal.* 37 (1), 55–70. doi:10.1007/s11244-006-0002-0

Hochman, G., Goldman, A. S., Felder, F. A., Mayer, J. M., Miller, A. J. M., Holland, P. L., et al. (2020). Potential economic feasibility of direct electrochemical nitrogen reduction as a route to ammonia. *ACS Sustain. Chem. Eng.* 8 (24), 8938–8948. doi:10.1021/acssuschemeng.0c01206

Hongda Li, H., Gu, S., Sun, Z., Guo, F., Xie, Y., Tao, B., et al. (2020). The in-built bionic "MoFe cofactor" in Fe-doped two-dimensional $MoTe_2$ nanosheets for boosting the photocatalytic nitrogen reduction performance. *J. Mat. Chem. A* 8 (26), 13038–13048. doi:10.1039/d0ta04251j

Horn, M. R., Singh, A., Alomari, S., Goberna-Ferrón, S., Benages-Vilau, R., Chodankar, N., et al. (2021). Polyoxometalates (POMs): From electroactive clusters to energy materials. *Energy Environ. Sci.* 14 (4), 1652–1700. doi:10.1039/D0EE03407J

Hou, T. T., Xiao, Y., Cui, P. X., Huang, Y., Tan, X. P., Zheng, X. S., et al. (2019). Operando oxygen vacancies for enhanced activity and stability toward nitrogen photofixation. *Adv. Energy Mat.* 9 (43), 1902319. doi:10.1002/aenm.201902319

Hu, K., Huang, Z., Zeng, L., Zhang, Z., Mei, L., Chai, Z., et al. (2022). Recent advances in MOF-based materials for photocatalytic nitrogen fixation. *Eur. J. Inorg. Chem.* 2022 (3), e202100748. doi:10.1002/ejic.202100748

Huang, L., Wu, J., Han, P., Al-Enizi, A. M., Almutairi, T. M., Zhang, L., et al. (2019). NbO_2 electrocatalyst toward 32% faradaic efficiency for N_2 fixation. *Small Methods* 3 (6), 1800386. doi:10.1002/smtd.201800386

Huang, Y., Zhang, N., Wu, Z., and Xie, X. (2020). Artificial nitrogen fixation over bismuth-based photocatalysts: Fundamentals and future perspectives. *J. Mat. Chem. A* 8 (10), 4978–4995. doi:10.1039/C9TA13589H

Hui, X., Li, L., Xia, Q., Hong, S., Hao, L., Robertson, A. W., et al. (2022). Interface engineered $Sb_2O_3/W_{18}O_{49}$ heterostructure for enhanced visible-light-driven photocatalytic N_2 reduction. *Chem. Eng. J.* 438, 135485. doi:10.1016/j.cej.2022.135485

Huimin Liu, H., Guijarro, N., and Luo, J. (2021). The pitfalls in electrocatalytic nitrogen reduction for ammonia synthesis. *J. Energy Chem.* 61, 149–154. doi:10.1016/j.jechem.2021.01.039

Jacobsen, C. J., Dahl, S., Clausen, B. S., Bahn, S., Logadottir, A., Nørskov, J. K., et al. (2001). Catalyst design by interpolation in the periodic table: Bimetallic ammonia synthesis catalysts. *J. Am. Chem. Soc.* 123 (34), 8404–8405. doi:10.1021/ja010963d

Jia, H. P., and Quadrelli, E. A. (2014). Mechanistic aspects of dinitrogen cleavage and hydrogenation to produce ammonia in catalysis and organometallic chemistry: Relevance of metal hydride bonds and dihydrogen. *Chem. Soc. Rev.* 43 (2), 547–564. doi:10.1039/C3CS60206K

Kitano, M., Inoue, Y., Yamazaki, Y., Hayashi, F., Kanbara, S., Matsuishi, S., et al. (2012). Ammonia synthesis using a stable electride as an electron donor and reversible hydrogen store. *Nat. Chem.* 4 (11), 934–940. doi:10.1038/nchem.1476

Kong, W., Liu, Z., Han, J., Xia, L., Wang, Y., Liu, Q., et al. (2019). Ambient electrochemical N_2-to-NH_3 fixation enabled by Nb_2O_5 nanowire array. *Inorg. Chem. Front.* 6 (2), 423–427. doi:10.1039/C8QI01049H

Kramm, U. I., Marschall, R., and Rose, M. (2019). Pitfalls in heterogeneous thermal, electro-and photocatalysis. *ChemCatChem* 11 (11), 2563–2574. doi:10.1002/cctc.201900137

Lee, J., Tan, L. L., and Chai, S. P. (2021). Heterojunction photocatalysts for artificial nitrogen fixation: Fundamentals, latest advances and future perspectives. *Nanoscale* 13 (15), 7011–7033. doi:10.1039/d1nr00783a

Lei, W., Xiao, J.-L., Liu, H.-P., Jia, Q.-L., and Zhang, H.-J. (2020). Tungsten disulfide: Synthesis and applications in electrochemical energy storage and conversion. *Tungsten* 2 (3), 217–239. doi:10.1007/s42864-020-00054-6

Li, X., Sun, X., Zhang, L., Sun, S., and Wang, W. (2018). Efficient photocatalytic fixation of N_2 by KOH-treated g-C_3N_4. *J. Mat. Chem. A* 6 (7), 3005–3011. doi:10.1039/C7TA09762J

Li, J., Chen, R., Wang, J., Zhou, Y., Yang, G., Dong, F., et al. (2022a). Subnanometric alkaline-earth oxide clusters for sustainable nitrate to ammonia photosynthesis. *Nat. Commun.* 13 (1), 1098. doi:10.1038/s41467-022-28740-8

Li, J., Lou, Z., and Li, B. (2022b). Nanostructured materials with localized surface plasmon resonance for photocatalysis. *Chin. Chem. Lett.* 33 (3), 1154–1168. doi:10.1016/j.cclet.2021.07.059

Liang Yang, L., Choi, C., Hong, S., Liu, Z., Zhao, Z., Yang, M., et al. (2020). Single yttrium sites on carbon-coated TiO_2 for efficient electrocatalytic N_2 reduction. *Chem. Commun.* 56 (74), 10910–10913. doi:10.1039/D0CC01136C

Libo Wang, L., Zhang, Q., Wei, T., Li, F., Sun, Z., Xu, L., et al. (2021). WC and cobalt nanoparticles embedded in nitrogen-doped carbon 3D nanocage derived from $H_3PW_{12}O_{40}$@ZIF-67 for photocatalytic nitrogen fixation. *J. Mat. Chem. A* 9 (5), 2912–2918. doi:10.1039/D0TA10303A

Lin Liu, L., Liu, J., Sun, K., Wan, J., Fu, F., Fan, J., et al. (2021). Novel phosphorus-doped Bi_2WO_6 monolayer with oxygen vacancies for superior photocatalytic water detoxication and nitrogen fixation performance. *Chem. Eng. J.* 411, 128629. doi:10.1016/j.cej.2021.128629

Lin Wang, L., Li, X., Hao, L., Hong, S., Robertson, A. W., Sun, Z., et al. (2022). Integration of ultrafine CuO nanoparticles with two-dimensional MOFs for enhanced electrochemicgal CO_2 reduction to ethylene. *Chin. J. Catal.* 43 (4), 1049–1057. doi:10.1016/S1872-2067(21)63947-5

Lindley, B. M., Appel, A. M., Krogh-Jespersen, K., Mayer, J. M., and Miller, A. J. (2016). Evaluating the thermodynamics of electrocatalytic N_2 reduction in acetonitrile. *ACS Energy Lett.* 1 (4), 698–704. doi:10.1021/acsenergylett.6b00319

Linsebigler, A. L., Lu, G., and Yates, J. T., Jr (1995). Photocatalysis on TiO_2 surfaces: Principles, mechanisms, and selected results. *Chem. Rev.* 95 (3), 735–758. doi:10.1021/cr00035a013

Liu, J., Zhang, Y., Lu, L., Wu, G., and Chen, W. (2012). Self-regenerated solar-driven photocatalytic water-splitting by urea derived graphitic carbon nitride with platinum nanoparticles. *Chem. Commun.* 48 (70), 8826. doi:10.1039/C2CC33644H

Liu, J., Kelley, M. S., Wu, W., Banerjee, A., Douvalis, A. P., Wu, J., et al. (2016). Nitrogenase-mimic iron-containing chalcogels for photochemical reduction of dinitrogen to ammonia. *Proc. Natl. Acad. Sci. U. S. A.* 113(20), 5530–5535. doi:10.1073/pnas.1605512113

Liu, Y., Cheng, M., He, Z., Gu, B., Xiao, C., Zhou, T., et al. (2019). Pothole-rich ultrathin WO_3 nanosheets that trigger N≡N bond activation of nitrogen for direct nitrate photosynthesis. *Angew. Chem. Int. Ed.* 58 (3), 731–735. doi:10.1002/anie.201808177

Liu, X., Luo, Y., Ling, C., Shi, Y., Zhan, G., Li, H., et al. (2022). Rare Earth La single atoms supported MoO_{3-x} for efficient photocatalytic nitrogen fixation. *Appl. Catal. B Environ.* 301, 120766. doi:10.1016/j.apcatb.2021.120766

Lu, H., Zhao, Y.-M., Saji, S. E., Yin, X., Wibowo, A., Tang, C. S., et al. (2022). All room-temperature synthesis, N_2 photofixation and reactivation over 2D cobalt oxides. *Appl. Catal. B Environ.* 304, 121001. doi:10.1016/j.apcatb.2021.121001

Luo, J., Bai, X., Li, Q., Yu, X., Li, C., Wang, Z., et al. (2019). Band structure engineering of bioinspired Fe doped $SrMoO_4$ for enhanced photocatalytic nitrogen reduction performance. *Nano Energy* 66, 104187. doi:10.1016/j.nanoen.2019.104187

Lv, C., Yan, C., Chen, G., Ding, Y., Sun, J., Zhou, Y., et al. (2018). An amorphous noble-metal-free electrocatalyst that enables nitrogen fixation under ambient conditions. *Angew. Chem. Int. Ed.* 57 (21), 6073–6076. doi:10.1002/anie.201801538

Mansingh, S., Das, K. K., Sultana, S., and Parida, K. (2021). Recent advances in wireless photofixation of dinitrogen to ammonia under the ambient condition: A review. *J. Photochem. Photobiol. C Photochem. Rev.* 47, 100402. doi:10.1016/j.jphotochemrev.2021.100402

Mao, Y., Yang, X., Gong, W., Zhang, J., Pan, T., Sun, H., et al. (2020). A dopant replacement-driven molten salt method toward the synthesis of sub-5-nm-sized ultrathin nanowires. *Small* 16 (23), 2001098. doi:10.1002/smll.202001098

Medford, A. J., and Hatzell, M. C. (2017). Photon-driven nitrogen fixation: Current progress, thermodynamic considerations, and future outlook. *ACS Catal.* 7 (4), 2624–2643. doi:10.1021/acscatal.7b00439

Meng, Q., Lv, C., Sun, J., Hong, W., Xing, W., Qiang, L., et al. (2019). High-efficiency Fe-mediated Bi_2MoO_6 nitrogen-fixing photocatalyst: Reduced surface work function and ameliorated surface reaction. *Appl. Catal. B Environ.* 256, 117781. doi:10.1016/j.apcatb.2019.117781

Meng, S.-L., Li, X.-B., Tung, C.-H., and Wu, L.-Z. (2021). Nitrogenase inspired artificial photosynthetic nitrogen fixation. *Chem* 7 (6), 1431–1450. doi:10.1016/j.chempr.2020.11.002

Meng Yang, M., Huo, R. P., Shen, H. D., Xia, Q. N., Qiu, J. S., Robertson, A. W., et al. (2020). Metal-tuned $W_{18}O_{49}$ for efficient electrocatalytic N_2 reduction. *ACS Sustain. Chem. Eng.* 8 (7), 2957–2963. doi:10.1021/acssuschemeng.9b07526

Mingli Zhang, M., Choi, C., Huo, R., Gu, G. H., Hong, S., Yan, C., et al. (2020). Reduced graphene oxides with engineered defects enable efficient electrochemical reduction of dinitrogen to ammonia in wide pH range. *Nano Energy* 68, 104323. doi:10.1016/j.nanoen.2019.104323

Montoya, J. H., Tsai, C., Vojvodic, A., and Nørskov, J. K. (2015). The challenge of electrochemical ammonia synthesis: A new perspective on the role of nitrogen scaling relations. *ChemSusChem* 8 (13), 2180–2186. doi:10.1002/cssc.201500322

Mou, H., Wang, J., Yu, D., Zhang, D., Chen, W., Wang, Y., et al. (2019). Fabricating amorphous g-C_3N_4/ZrO_2 photocatalysts by one-step pyrolysis for solar-driven ambient ammonia synthesis. *ACS Appl. Mat. Interfaces* 11 (47), 44360–44365. doi:10.1021/acsami.9b16432

Mousavi, M., Habibi, M. M., Zhang, G., Pourhakkak, P., moradian, S., Ghasemi, J. B., et al. (2022). *In-situ* construction of ZnO/Sb_2MoO_6 nano-heterostructure for efficient visible-light photocatalytic conversion of N_2 to NH_3. *Surf. Interfaces* 30, 101844. doi:10.1016/j.surfin.2022.101844

Ning Zhang, N., Jalil, A., Wu, D. X., Chen, S. M., Liu, Y. F., Gao, C., et al. (2018). Refining defect states in $W_{18}O_{49}$ by Mo doping: A strategy for tuning N_2 activation towards solar-driven nitrogen fixation. *J. Am. Chem. Soc.* 140 (30), 9434–9443. doi:10.1021/jacs.8b02076

Nunes, B. N., Lopes, O. F., Patrocinio, A. O. T., and Bahnemann, D. W. (2020). Recent advances in niobium-based materials for photocatalytic solar fuel production. *Catalysts* 10 (1), 126. doi:10.3390/catal10010126

Oshikiri, T., Ueno, K., and Misawa, H. (2016). Selective dinitrogen conversion to ammonia using water and visible light through plasmon-induced charge separation. *Angew. Chem. Int. Ed.* 55 (12), 3942–3946. doi:10.1002/anie.201511189

Qin, J., Zhao, W., Hu, X., Li, J., Ndokoye, P., and Liu, B. (2021). Exploring the N_2 adsorption and activation mechanisms over the 2H/1T Mixed-phase ultrathin $Mo_{1-x}W_xS_2$ nanosheets for boosting N_2 photosynthesis. *ACS Appl. Mater. Interfaces.* 13 (6), 7127–7134. doi:10.1021/acsami.0c19282

Qiu, P., Huang, C., Dong, G., Chen, F., Zhao, F., Yu, Y., et al. (2021). Plasmonic gold nanocrystals simulated efficient photocatalytic nitrogen fixation over Mo doped $W_{18}O_{49}$ nanowires. *J. Mat. Chem. A* 9 (25), 14459–14465. doi:10.1039/D1TA03339E

Ren, W., Mei, Z., Zheng, S., Li, S., Zhu, Y., Zheng, J., et al. (2020). Wavelength-dependent solar N_2 fixation into ammonia and nitrate in pure water. *Research* 2020, 1–12. doi:10.34133/2020/3750314

Rong Zhang, R., Guo, H., Yang, L., Wang, Y., Niu, Z., Huang, H., et al. (2019). Electrocatalytic N_2 fixation over hollow VO_2 microspheres at ambient conditions. *ChemElectroChem* 6 (4), 1014–1018. doi:10.1002/celc.201801484

Schrauzer, G. N., and Guth, T. D. (1977). Photolysis of water and photoreduction of nitrogen on titanium dioxide. *J. Am. Chem. Soc.* 99 (22), 7189–7193. doi:10.1021/ja00464a015

Schrauzer, G., and Guth, T. (2002). Photolysis of water and photoreduction of nitrogen on titanium dioxide. *J. Am. Chem. Soc.* 99 (22), 7189–7193. doi:10.1021/ja00464a015

Shen, H., Peppel, T., Strunk, J., and Sun, Z. (2020). Photocatalytic reduction of CO_2 by metal-free-based materials: Recent advances and future perspective. *Sol. RRL* 4 (8), 1900546. doi:10.1002/solr.201900546

Shen, H., Yang, M., Hao, L., Wang, J., Strunk, J., Sun, Z., et al. (2021). Photocatalytic nitrogen reduction to ammonia: Insights into the role of defect engineering in photocatalysts. *Nano Res.* 15, 2773–2809. doi:10.1007/s12274-021-3725-0

Shende, A. G., Tiwari, C. S., Bhoyar, T. H., Vidyasagar, D., and Umare, S. S. (2019). BWO nano-octahedron coupled with layered g-C_3N_4: An efficient visible light active photocatalyst for degradation of cationic/anionic dyes, and N_2 reduction. *J. Mol. Liq.* 296, 111771. doi:10.1016/j.molliq.2019.111771

Shi, R., Zhao, Y., Waterhouse, G. I. N., Zhang, S., and Zhang, T. (2019). Defect engineering in photocatalytic nitrogen fixation. *ACS Catal.* 9 (11), 9739–9750. doi:10.1021/acscatal.9b03246

Shi, L., Yin, Y., Wang, S., and Sun, H. (2020a). Rational catalyst design for N_2 reduction under ambient conditions: Strategies toward enhanced conversion efficiency. *ACS Catal.* 10 (12), 6870–6899. doi:10.1021/acscatal.0c01081

Shi, L., Li, Z., Ju, L., Carrasco-Pena, A., Orlovskaya, N., Zhou, H., et al. (2020b). Promoting nitrogen photofixation over a periodic WS_2@TiO_2 nanoporous film. *J. Mat. Chem. A* 8 (3), 1059–1065. doi:10.1039/C9TA12743G

Shipman, M. A., and Symes, M. D. (2017). Recent progress towards the electrosynthesis of ammonia from sustainable resources. *Catal. Today* 286, 57–68. doi:10.1016/j.cattod.2016.05.008

Shiraishi, Y., Shiota, S., Kofuji, Y., Hashimoto, M., Chishiro, K., Hirakawa, H., et al. (2018). Nitrogen fixation with water on carbon-nitride-based metal-free photocatalysts with 0.1% solar-to-ammonia energy conversion efficiency. *ACS Appl. Energy Mat.* 1 (8), 4169–4177. doi:10.1021/acsaem.8b00829

Shuai Zhang, S., Zhao, Y., Shi, R., Waterhouse, G. I., and Zhang, T. (2019). Photocatalytic ammonia synthesis: Recent progress and future. *EnergyChem* 1 (2), 100013. doi:10.1016/j.enchem.2019.100013

Skúlason, E., Bligaard, T., Gudmundsdóttir, S., Studt, F., Rossmeisl, J., Abild-Pedersen, F., et al. (2012). A theoretical evaluation of possible transition metal electro-catalysts for N_2 reduction. *Phys. Chem. Chem. Phys.* 14 (3), 1235–1245. doi:10.1039/C1CP22271F

Song, J., Huang, Z.-F., Pan, L., Zou, J.-J., Zhang, X., Wang, L., et al. (2015). Oxygen-deficient tungsten oxide as versatile and efficient hydrogenation catalyst. *ACS Catal.* 5 (11), 6594–6599. doi:10.1021/acscatal.5b01522

Su, S., Li, X., Zhang, X., Zhu, J., Liu, G., Tan, M., et al. (2022). Keggin-type SiW_{12} encapsulated in MIL-101(Cr) as efficient heterogeneous photocatalysts for nitrogen fixation reaction. *J. Colloid Interface Sci.* 621, 406–415. doi:10.1016/j.jcis.2022.04.006

Sun, S., Li, X., Wang, W., Zhang, L., and Sun, X. (2017). Photocatalytic robust solar energy reduction of dinitrogen to ammonia on ultrathin MoS_2. *Appl. Catal. B Environ.* 200, 323–329. doi:10.1016/j.apcatb.2016.07.025

Sun, Z., Talreja, N., Tao, H., Texter, J., Muhler, M., Strunk, J., et al. (2018). Catalysis of carbon dioxide photoreduction on nanosheets: Fundamentals and challenges. *Angew. Chem. Int. Ed.* 57 (26), 7610–7627. doi:10.1002/anie.201710509

Sun, Z., Huo, R., Choi, C., Hong, S., Wu, T.-S., Qiu, J., et al. (2019). Oxygen vacancy enables electrochemical N_2 fixation over WO_3 with tailored structure. *Nano Energy* 62, 869–875. doi:10.1016/j.nanoen.2019.06.019

Sun, D., Bai, H., Zhao, Y., Zhang, Q., Bai, Y., Liu, Y., et al. (2020). Amorphous $MnCO_3$/C double layers decorated on $BiVO_4$ photoelectrodes to boost nitrogen reduction. *ACS Appl. Mat. Interfaces* 12 (47), 52763–52770. doi:10.1021/acsami.0c16337

Swain, G., Sultana, S., and Parida, K. (2020). Constructing a novel surfactant-free MoS_2 nanosheet modified $MgIn_2S_4$ marigold microflower: An efficient visible-light driven 2D-2D p-n heterojunction photocatalyst toward HER and pH regulated NRR. *ACS Sustain. Chem. Eng.* 8 (12), 4848–4862. doi:10.1021/acssuschemeng.9b07821

Tang, C., and Qiao, S.-Z. (2019). How to explore ambient electrocatalytic nitrogen reduction reliably and insightfully. *Chem. Soc. Rev.* 48 (12), 3166–3180. doi:10.1039/C9CS00280D

Tao, H., Choi, C., Ding, L.-X., Jiang, Z., Han, Z., Jia, M., et al. (2019). Nitrogen fixation by Ru single-atom electrocatalytic reduction. *Chem* 5 (1), 204–214. doi:10.1016/j.chempr.2018.10.007

Tianyu Wang, T., Feng, C., Liu, J., Wang, D., Hu, H., Hu, J., et al. (2021). Bi_2WO_6 hollow microspheres with high specific surface area and oxygen vacancies for efficient photocatalysis N_2 fixation. *Chem. Eng. J.* 414, 128827. doi:10.1016/j.cej.2021.128827

Tianyu Wang, T., Liu, J., Wu, P., Feng, C., Wang, D., Hu, H., et al. (2020). Direct utilization of air and water as feedstocks in the photo-driven nitrogen reduction reaction over a ternary Z-scheme SiW_9Co_3/PDA/BWO hetero-junction. *J. Mat. Chem. A* 8 (32), 16590–16598. doi:10.1039/C9TA13902H

Tong Xu, T., Ma, B., Liang, J., Yue, L., Liu, Q., Li, T., et al. (2021). Recent progress in metal-free electrocatalysts toward ambient N_2 reduction reaction. *Acta Phys. -Chim. Sin.* 37 (7), 2009043. doi:10.3866/pku.Whxb202009043

Utomo, W. P., Leung, M. K. H., Yin, Z., Wu, H., and Ng, Y. H. (2022). Advancement of bismuth-based materials for electrocatalytic and photo(electro) catalytic ammonia synthesis. *Adv. Funct. Mat.* 32 (4), 2106713. doi:10.1002/adfm.202106713

van der Ham, C. J. M., Koper, M. T. M., and Hetterscheid, D. G. H. (2014). Challenges in reduction of dinitrogen by proton and electron transfer. *Chem. Soc. Rev.* 43 (15), 5183–5191. doi:10.1039/C4CS00085D

Vesali-Kermani, E., Habibi-Yangjeh, A., Diarmand-Khalilabad, H., and Ghosh, S. (2020a). Nitrogen photofixation ability of g-C_3N_4 nanosheets/Bi_2MoO_6 heterojunction photocatalyst under visible-light illumination. *J. Colloid Interface Sci.* 563, 81–91. doi:10.1016/j.jcis.2019.12.057

Vesali-Kermani, E., Habibi-Yangjeh, A., and Ghosh, S. (2020b). Efficiently enhanced nitrogen fixation performance of g-C_3N_4 nanosheets by decorating $Ni_3V_2O_8$ nanoparticles under visible-light irradiation. *Ceram. Int.* 46 (15), 24472–24482. doi:10.1016/j.ceramint.2020.06.232

Wen Zhao, W., Qin, J., Teng, W., Mu, J., Chen, C., Ke, J., et al. (2022). Catalytic photo-redox of simulated air into ammonia over bimetallic MOFs nanosheets with oxygen vacancies. *Appl. Catal. B Environ.* 305, 121046. doi:10.1016/j.apcatb.2021.121046

Wenjie Liu, W., Yin, K., Yuan, K., Zuo, S., Yang, S., Yao, C., et al. (2020). *In situ* synthesis of Bi_2MoO_6@C@attapulgite photocatalyst for enhanced photocatalytic nitrogen fixation ability under simulated solar irradiation. *Colloids Surfaces A Physicochem. Eng. Aspects* 591, 124488. doi:10.1016/j.colsurfa.2020.124488

Xiao, C., Zhang, L., Wang, K., Wang, H., Zhou, Y., Wang, W., et al. (2018). A new approach to enhance photocatalytic nitrogen fixation performance via phosphate-bridge: A case study of SiW_{12}/K-C_3N_4. *Appl. Catal. B Environ.* 239, 260–267. doi:10.1016/j.apcatb.2018.08.012

Xiao-Fei Li, X.-F., Li, Q.-K., Cheng, J., Liu, L., Yan, Q., Wu, Y., et al. (2016). Conversion of dinitrogen to ammonia by FeN_3-embedded graphene. *J. Am. Chem. Soc.* 138 (28), 8706–8709. doi:10.1021/jacs.6b04778

Xiao-Hong Li, X.-H., Chen, W.-L., Tan, H.-Q., Li, F.-R., Li, J.-P., Li, Y.-G., et al. (2019). Reduced state of the graphene oxide@polyoxometalate nanocatalyst achieving high-efficiency nitrogen fixation under light driving conditions. *ACS Appl. Mat. Interfaces* 11 (41), 37927–37938. doi:10.1021/acsami.9b12328

Xiao-Hong Li, X.-H., He, P., Wang, T., Zhang, X.-W., Chen, W.-L., Li, Y.-G., et al. (2020). Keggin-type polyoxometalate-based ZIF-67 for enhanced photocatalytic nitrogen fixation. *ChemSusChem* 13 (10), 2769–2778. doi:10.1002/cssc.202000328

Xiazhang Li, X., He, C., Dai, D., Zuo, S., Yan, X., Yao, C., et al. (2020). Nano-mineral induced nonlinear optical $LiNbO_3$ with abundant oxygen vacancies for photocatalytic nitrogen fixation: Boosting effect of polarization. *Appl. Nanosci.* 10 (9), 3477–3490. doi:10.1007/s13204-020-01443-6

Xin Liu, X., Gu, S., Zhao, Y., Zhou, G., and Li, W. (2020). $BiVO_4$, Bi_2WO_6 and Bi_2MoO_6 photocatalysis: A brief review. *J. Mat. Sci. Technol.* 56, 45–68. doi:10.1016/j.jmst.2020.04.023

Xin Wang, X., Feng, Z., Xiao, B., Zhao, J., Ma, H., Tian, Y., et al. (2020). Polyoxometalate-based metal-organic framework-derived bimetallic hybrid materials for upgraded electrochemical reduction of nitrogen. *Green Chem.* 22 (18), 6157–6169. doi:10.1039/D0GC01149E

Xing, P., Chen, P., Chen, Z., Hu, X., Lin, H., Wu, Y., et al. (2018). Novel ternary MoS_2/C-ZnO composite with efficient performance in photocatalytic NH_3 synthesis under simulated sunlight. *ACS Sustain. Chem. Eng.* 6 (11), 14866–14879. doi:10.1021/acssuschemeng.8b03388

Xing, P., Wu, S., Chen, Y., Chen, P., Hu, X., Lin, H., et al. (2019). New application and excellent performance of Ag/$KNbO_3$ nanocomposite in photocatalytic NH_3 synthesis. *ACS Sustain. Chem. Eng.* 7 (14), acssuschemeng.9b01938. doi:10.1021/acssuschemeng.9b01938

Xing, P., Zhang, W., Chen, L., Dai, X., Zhang, J., Zhao, L., et al. (2020). Preparation of a NiO/$KNbO_3$ nanocomposite via a photodeposition method and its superior performance in photocatalytic N_2 fixation. *Sustain. Energy Fuels* 4 (3), 1112–1117. doi:10.1039/C9SE01003C

Xu, T., Ma, D., Li, C., Liu, Q., Lu, S., Asiri, A. M., et al. (2020). Ambient electrochemical NH_3 synthesis from N_2 and water enabled by ZrO_2 nanoparticles. *Chem. Commun.* 56 (25), 3673–3676. doi:10.1039/C9CC10087C

Xu, H., Ma, Y., Chen, J., Zhang, W., and Yang, J. (2022). Electrocatalytic reduction of nitrate – A step towards a sustainable nitrogen cycle. *Chem. Soc. Rev.* 51, 2710–2758. doi:10.1039/D1CS00857A

Xu, Y., and Schoonen, M. A. (2000). The absolute energy positions of conduction and valence bands of selected semiconducting minerals. *Am. Mineral.* 85 (3-4), 543–556. doi:10.2138/am-2000-0416

Xue Chen, X., Li, J.-Y., Tang, Z.-R., and Xu, Y.-J. (2020). Surface-defect-engineered photocatalyst for nitrogen fixation into value-added chemical feedstocks. *Catal. Sci. Technol.* 10 (18), 6098–6110. doi:10.1039/d0cy01227k

Xue, X., Chen, R., Yan, C., Hu, Y., Zhang, W., Yang, S., et al. (2019). Efficient photocatalytic nitrogen fixation under ambient conditions enabled by the heterojunctions of n-type Bi_2MoO_6 and oxygen-vacancy-rich p-type BiOBr. *Nanoscale* 11 (21), 10439–10445. doi:10.1039/C9NR02279A

Xuerui Zhang, X., Shi, R., Li, Z., Zhao, J., Huang, H., Zhou, C., et al. (2022). Photothermal-assisted photocatalytic nitrogen oxidation to nitric acid on palladium-decorated titanium oxide. *Adv. Energy Mat.* 12, 2103740. doi:10.1002/aenm.202103740

Yang, J., Bai, H., Guo, Y., Zhang, H., Jiang, R., Yang, B., et al. (2021). Photodriven disproportionation of nitrogen and its change to reductive nitrogen photofixation. *Angew. Chem. Int. Ed.* 60 (2), 927–936. doi:10.1002/anie.202010192

Yehuan Li, Y., Chen, X., Zhang, M., Zhu, Y., Ren, W., Mei, Z., et al. (2019). Oxygen vacancy-rich MoO_{3-x} nanobelts for photocatalytic N_2 reduction to NH_3 in pure water. *Catal. Sci. Technol.* 9 (3), 803–810. doi:10.1039/C8CY02357C

Yi-Fei Zhang, Y.-F., Zhu, Y.-K., Lv, C.-X., Lai, S.-J., Xu, W.-J., Sun, J., et al. (2020). Enhanced visible-light photoelectrochemical performance via chemical vapor deposition of Fe_2O_3 on a WO_3 film to form a heterojunction. *Rare Met.* 39 (7), 841–849. doi:10.1007/s12598-019-01311-5

Yifu Chen, Y., Liu, H., Ha, N., Licht, S., Gu, S., Li, W., et al. (2020). Revealing nitrogen-containing species in commercial catalysts used for ammonia electrosynthesis. *Nat. Catal.* 3 (12), 1055–1061. doi:10.1038/s41929-020-00527-4

Yin, S., and Asakura, Y. (2019). Recent research progress on mixed valence state tungsten based materials. *Tungsten* 1 (1), 5–18. doi:10.1007/s42864-019-00001-0

Yin, Y., Jiang, M., and Liu, C. (2018). DFT study of POM-supported single atom catalyst (M_1/POM, M = Ni, Pd, Pt, Cu, Ag, Au, POM = $[PW_{12}O_{40}]^{3-}$) for activation of nitrogen molecules. *Acta Phys. -Chim. Sin.* 34 (3), 270–277. doi:10.3866/pku.Whxb201707071

Ying, Z., Chen, S., Zhang, S., Peng, T., and Li, R. (2019). Efficiently enhanced N_2 photofixation performance of sea-urchin-like $W_{18}O_{49}$ microspheres with Mn-doping. *Appl. Catal. B Environ.* 254, 351–359. doi:10.1016/j.apcatb.2019.05.005

Yuan Feng, Y., zhao, Z., Wang, T., Li, J., Xu, M., Jiao, H., et al. (2022). Magnetic field-enhanced photocatalytic nitrogen fixation over defect-rich ferroelectric Bi_2WO_6. *Ceram. Int.* 48, 20062–20069. doi:10.1016/j.ceramint.2022.03.282

Yuan, J., Yi, X., Tang, Y., Liu, M., and Liu, C. (2020). Efficient photocatalytic nitrogen fixation: Enhanced polarization, activation, and cleavage by asymmetrical electron donation to N≡N bond. *Adv. Funct. Mater.* 30 (4), 1906983. doi:10.1002/adfm.201906983

Yuhua Wang, Y. H., Liu, T. Y., Li, H. H., Liu, B., and Yang, L. F. (2019). Tungsten-based photocatalysts with UV–Vis–NIR photocatalytic capacity: Progress and opportunity. *Tungsten* 1 (4), 247–257. doi:10.1007/s42864-020-00031-z

Yuting Wang, Y., Li, H., Zhou, W., Zhang, X., Zhang, B., Yu, Y., et al. (2022). Structurally disordered RuO_2 nanosheets with rich oxygen vacancies for enhanced nitrate electroreduction to ammonia. *Angew. Chem. Int. Ed. Engl.* 61, e202202604. doi:10.1002/anie.202202604

Yuxin Liu, Y., Xue, Y., Hui, L., Yu, H., Fang, Y., He, F., et al. (2021). Porous graphdiyne loading CoO_x quantum dots for fixation nitrogen reaction. *Nano Energy* 89, 106333. doi:10.1016/j.nanoen.2021.106333

Zejian Wang, J. H., Ng, Sue-Faye, Wen, Liu, Huang, Junjie, Chen, Pengfei, and Ong, Wee-Jun (2021). Recent progress of perovskite oxide in emerging photocatalysis landscape: Water splitting, CO_2 reduction, and N_2 fixation. *Acta Phys. -Chim. Sin.* 37 (6), 2011033. doi:10.3866/pku.Whxb202011033

Zhang, Y., Yu, J., Yu, D., Zhou, X., and Lu, W. (2011). Enhancement in the photocatalytic and photoelectrochemical properties of visible-light driven $BiVO_4$ photocatalyst. *Rare Met.* 30 (1), 192–198. doi:10.1007/s12598-011-0267-8

Zhang, L., Mohamed, H. H., Dillert, R., and Bahnemann, D. (2012). Kinetics and mechanisms of charge transfer processes in photocatalytic systems: A review. *J. Photochem. Photobiol. C Photochem. Rev.* 13 (4), 263–276. doi:10.1016/j.jphotochemrev.2012.07.002

Zhang, Y., Dong, N., Tao, H., Yan, C., Huang, J., Liu, T., et al. (2017). Exfoliation of stable 2D black phosphorus for device fabrication. *Chem. Mat.* 229, 66445–66456. doi:10.1021/acs.chemmater.7b01991

Zhang, G., Meng, Y., Xie, B., Ni, Z., Lu, H., Xia, S., et al. (2021). Precise location and regulation of active sites for highly efficient photocatalytic synthesis of ammonia by facet-dependent $BiVO_4$ single crystals. *Appl. Catal. B Environ.* 296, 120379. doi:10.1016/j.apcatb.2021.120379

Zhao, W., Xi, H., Zhang, M., Li, Y., Chen, J., Zhang, J., et al. (2015). Enhanced quantum yield of nitrogen fixation for hydrogen storage with *in situ*-formed carbonaceous radicals. *Chem. Commun.* 51 (23), 4785–4788. doi:10.1039/C5CC00589B

Zhao, Y., Shi, R., Bian, X., Zhou, C., Zhao, Y., Zhang, S., et al. (2019). Ammonia detection methods in photocatalytic and electrocatalytic experiments: How to improve the reliability of NH_3 production rates? *Adv. Sci.* 6 (8), 1802109. doi:10.1002/advs.201802109

Zhao, Z. Q., Choi, C., Hong, S., Shen, H. D., Yan, C., Masa, J., et al. (2020). Surface-engineered oxidized two-dimensional Sb for efficient visible light-driven N_2 fixation. *Nano Energy* 78, 105368. doi:10.1016/j.nanoen.2020.105368

Zhao, Y., Wu, F., Miao, Y., Zhou, C., Xu, N., Shi, R., et al. (2021). Revealing ammonia quantification minefield in photo/electrocatalysis. *Angew. Chem. Int. Ed.* 60 (40), 21728–21731. doi:10.1002/anie.202108769

Zhen Zhao, Z., Park, J., Choi, C., Hong, S., Hui, X., Zhang, H., et al. (2022). Engineering vacancy and hydrophobicity of two-dimensional $TaTe_2$ for efficient and stable electrocatalytic N_2 reduction. *Innovation* 3 (1), 100190. doi:10.1016/j.xinn.2021.100190

Zheng, H., Ou, J. Z., Strano, M. S., Kaner, R. B., Mitchell, A., Kalantar-zadeh, K., et al. (2011). Nanostructured tungsten oxide–properties, synthesis, and applications. *Adv. Funct. Mat.* 21 (12), 2175–2196. doi:10.1002/adfm.201002477

Zheng, Q., Xu, Y., Wan, Y., Wu, J., Hu, X., Yao, X., et al. (2020). Synthesis of $CoFe_2O_4$-modified g-C_3N_4 with enhanced photocatalytic performance for nitrogen fixation. *J. Nanopart. Res.* 22 (9), 301. doi:10.1007/s11051-020-05028-w

Zheng, J., Lu, L., Lebedev, K., Wu, S., Zhao, P., McPherson, I. J., et al. (2021). Fe on molecular-layer MoS_2 as inorganic Fe-S_2-Mo motifs for light-driven nitrogen fixation to ammonia at elevated temperatures. *Chem. Catal.* 1 (1), 162–182. doi:10.1016/j.checat.2021.03.002

Zheng Wang, Z., Li, C., and Domen, K. (2019). Recent developments in heterogeneous photocatalysts for solar-driven overall water splitting. *Chem. Soc. Rev.* 48 (7), 2109–2125. doi:10.1039/C8CS00542G

Zhi-Yuan Wang, Z.-Y., Jiang, S.-D., Duan, C.-Q., Wang, D., Luo, S.-H., Liu, Y.-G., et al. (2020). *In situ* synthesis of Co_3O_4 nanoparticles confined in 3D nitrogen-doped porous carbon as an efficient bifunctional oxygen electrocatalyst. *Rare Met.* 39 (12), 1383–1394. doi:10.1007/s12598-020-01581-4

Zhou, S., Zhang, C., Liu, J., Liao, J., Kong, Y., Xu, Y., et al. (2019). Formation of an oriented Bi_2WO_6 photocatalyst induced by *in situ* Bi reduction and its use for efficient nitrogen fixation. *Catal. Sci. Technol.* 9 (20), 5562–5566. doi:10.1039/C9CY00972H

Zhou, X., Liu, H., Xia, B. Y., Ostrikov, K., Zheng, Y., Qiao, S.-Z., et al. (2022). Customizing the microenvironment of CO_2 electrocatalysis via three-phase interface engineering. *SmartMat* 3 (1), 111–129. doi:10.1002/smm2.1109

Zhu, D., Zhang, L., Ruther, R. E., and Hamers, R. J. (2013). Photo-illuminated diamond as a solid-state source of solvated electrons in water for nitrogen reduction. *Nat. Mat.* 12 (9), 836–841. doi:10.1038/nmat3696

Zhu, J., Chen, X., Thang, A. Q., Li, F.-L., Chen, D., Geng, H., et al. (2022). Vanadium-based metal-organic frameworks and their derivatives for electrochemical energy conversion and storage. *SmartMat*. doi:10.1002/smm2.1091

Ziegenbalg, D., Zander, J., and Marschall, R. (2021). Photocatalytic nitrogen reduction: Challenging materials with reaction engineering. *ChemPhotoChem* 5 (9), 792–807. doi:10.1002/cptc.202100084